TÉCNICO
LISBOA

Exploration of Model Updating Methods Based on GVT of a Blended Wing Body Configuration Aircraft

Hugo Miguel Candeias Faustino

Thesis to obtain the Master of Science Degree in

Aerospace Engineering

Supervisors: Prof. Afzal Suleman
Dr. José Lobo do Vale

Examination Committee

Chairperson: Prof. Fernando Lau
Supervisor: Prof. Afzal Suleman
Member of the Committee: Prof. Pedro Gamboa

December 2021

Declaration

I declare that this document is an original work of my own authorship and that it fulfills all the requirements of the Code of Conduct and Good Practices of the Universidade de Lisboa.

Acknowledgments

The present thesis comes together as a result of a marvelous seven-month experience in Victoria, BC, Canada. For this opportunity I thank my supervisor Professor Afzal Suleman. The exquisite team of engineers I was surrounded by and the teamwork spirit at University of Victoria's Centre for Aerospace Research are qualities I will always be grateful to have experienced during this period.

My words of gratitude intensify for Doctor José Vale. His co-supervision was pivotal throughout this thesis. A thank you to his tireless support, to his time spent guiding me and to his helpful corrections and recommendations.

Another special thank you goes to Stephen Warwick for his patience and availability to help with instrumentation and testing setup. Appreciation words for both Pedro Fernandes and Daniele Obertino for their support during testing days are also worth mentioning.

To my family, whose support was absolute during the years leading to this day, a warming recognition.

To a few friends in Portugal, with whom I had the pleasure of sharing my academic journey, Francisco Sargento, Olívia Pinto, Ana Veiga, Miguel Morgado and Sara Pessoa, my gratefulness.

Last but not least a special thank you to people I came across while in Canada and can now call friends, Joshua Yin and Rie Hata. My gratitude towards you is inestimable.

Resumo

Os elevados padrões exigidos pela indústria aeroespacial implicam a validação de conceitos e designs através de testes experimentais minuciosos. Este trabalho foca-se em Testes de Vibração em Solo, realizados num conceito *Blended Wing Body* e cujos resultados são usados para atualizar parâmetros estruturais de Modelos de Elementos Finitos simplificados.

O presente estudo foi realizado no *Centre for Aerospace Research* da Universidade de Victoria. Antes da fase de teste, uma análise de Atualização de Modelo foi conduzida a partir dos resultados experimentais obtidos para a asa da aeronave através do *FEMtools*.

Foi criada uma interface em *LabVIEW* para extrair dados das sessões experimentais e foi desenvolvido um modelo em *MEscope* capaz de animar estes dados, possibilitando ainda a extração dos parâmetros modais. Os resultados da Análise Modal foram então usados para o estudo da convergência das frequências e modos de vibração entre os dados experimentais e os do modelo analítico simplificado da aeronave.

Duas sessões de Testes de Vibração em Solo foram necessárias para recolher os dados e prosseguir com o estudo de atualização de modelo. A convergência da frequência foi novamente feita através do *FEMtools* mas os modos de vibração dinâmicos foram estudados a partir de um algoritmo de otimização desenvolvido em *MATLAB*.

Um Modelo de viga de Elementos Finitos foi gerado e mostrou-se capaz de replicar o comportamento da aeronave obtido experimentalmente ao nível das frequências naturais. Modelos mais complexos foram posteriormente criados para tentar reproduzir os modos de vibração, mostrando-se uma tarefa com alguns desafios.

Palavras-chave: Testes de Vibração em Solo, Modelos de Elementos Finitos, Atualização de Modelo, Análise Modal.

Abstract

The high standards the aerospace industry has to meet imply validation of concepts and designs by thoroughly testing them. This work focuses on Ground Vibration Testing, which is carried out on a Blended Wing Body concept and the data extracted used to update structural parameters of simplified Finite Element Models.

The study was conducted at University of Victoria's Centre for Aerospace Research. Prior to testing phase, an introductory Model Update analysis was done using *FEMtools* on previously obtained experimental results for the aircraft's wing.

A user interface to extract data from the test sessions was done in *LabVIEW* and a model to animate and extract modal parameters from was created in *MEscope*. The Modal Analysis results were then used to match the frequency and mode shapes between the experimental and an analytical simplified model of the aircraft.

Two sessions of Ground Vibration Tests were performed to collect all the needed data and proceed with the model updating study. This time, the frequency matching was made recurring to *FEMtools* but the dynamic mode shape study was done through an optimization algorithm developed in *MATLAB*.

A relatively simple beam Finite Element Model was generated and proved to accurately match the natural frequencies obtained experimentally. More complex models were then produced to mimic the mode shapes, which proved to be challenging.

x

Contents

List of Tables

List of Figures

Nomenclature

Greek symbols

ε Convergence margin.

ζ Damping.

π Pi (3.14159...)

ρ Mass density.

ψ Eigenvector.

ω Angular frequency.

Roman symbols

A Cross section area.

b Width of the wingbox.

C Damping matrix.

E Young's modulus.

f Frequency.

$\boldsymbol{f}$ Generalized force vector.

h Height of the wingbox.

I Moment of inertia.

j Imaginary unit.

K Stiffness matrix.

M Mass matrix.

m Mass.

t Time.

$\boldsymbol{u}$ Displacement vector.

$\dot{u}$ Velocity vector.

$\ddot{u}$ Acceleration vector.

Subscripts

a Analytical.

e Experimental.

i Mode shape number index.

x, y, z Cartesian components.

EMA   Relative to Experimental Modal Analysis.

FEA   Relative to Finite Element Analysis.

Superscripts

-1 Inverse.

*   Complex conjugate.

T   Transpose.

Acronyms

BA	Bombardier Aerospace.
BWB	Blended Wing Body.
CC	Correlation Coefficients.
CfAR	Centre for Aerospace Research.
CMIF	Complex Mode Indicator Function.
DOF	Degree of Freedom.
DV	Design Variable.
FE	Finite Element.
FEM	Finite Element Model.
FRF	Frequency Response Function.
GVT	Ground Vibration Test.
MAC	Modal Assurance Criterion.
MDOF	Multiple Degree of Freedom.
MPC	Multipoint Constraint.
RBM	Rigid Body Motion.
SDOF	Single Degree of Freedom.
TF	Transfer Function.
UVic	University of Victoria.

Chapter 1

Introduction

Whilst at the forefront of scientific research, aerospace related technologies redefine state-of-the-art knowledge time after time. This urge to push the boundaries arises from the extremely demanding requirements, with special commitment in current days towards efficiency and sustainability. Such high standards translate into nearly flawless flying machines, as the result of extensive research supported by vast theoretical background and consequent validation. The latter takes the form of computational analysis or experimental tests and support the proposed design.

Among the most promising configurations for air vehicles regarding aerodynamic efficiency one has the Blended Wing Body (BWB), and despite technical challenges on some areas of its design (namely on its stability and control), this concept also trumps the equivalent conventional transport aircraft when considering noise levels, weight and operating costs. Having the fuselage and wings combined into one smooth shape instead of three distinct assembled parts, the hybrid design resembles a flying wing, albeit incorporating features of conventional aircraft [1]. The lift to drag ratio is higher due to the reduced ratio of wetted area over reference area, representing a breakthrough in subsonic transport efficiency [2].

1.1 Motivation

The University of Victoria Centre for Aerospace Research (UVic CfAR), in a collaboration project with Bombardier Aerospace (BA), is responsible for the design, building and testing of a BWB prototype which, scaled at 16.5%, has 24 control surfaces and a wingspan of 5.4m. A smaller model, scaled at 7%, was also previously developed by CfAR and served the purpose of collecting in-flight data in order to improve and validate the control models used by the autopilot.

Ground Vibration Tests (GVTs) represent an essential milestone during the certification process for aircraft. Araújo [3] has previously performed both Static Load tests and GVTs on one of the wings of the BWB 16.5% prototype. He was also in charge of developing a beam Finite Element Model (FEM) which went through model updates that allowed the matching of the natural frequencies from the computational model to those obtained from the experimental data acquired during testing.

As the project unraveled, the need for performing GVT for the entire aircraft structure emerged for

both validation purposes and so that its structural dynamic models could be improved from the obtained experimental vibration data. These models are then used to study flutter behavior and to plan critical flight tests [4]. Being performed relatively late in the development cycle and when the availability of the aircraft is limited, the pressure to get the test results as quickly and efficiently as possible without compromising the accuracy of the results is quite high.

1.2 Topic Overview and State of the Art

Numerous unconventional configurations for aircraft have been explored and scrutinized in the past with the end goal of achieving a better and more efficient product in civil aviation.

In fact, the BWB configuration is not new. Even though not much success was ever obtained before, several attempts to make it thrive have been made. Newer iterations of this design include Airbus' MAVERIC and ZEROe concepts, as well as NASA's N3-X concept, illustrated in Fig.1.1. The fuel savings and often emissions and noise reductions due to the combining of electric propulsion with the BWB concept make it appealing for aerospace companies to try to push it to the limit of its potential — specially at a time when ecological concerns influence decisions people make on a daily basis.

(a) MAVERIC concept [5].   (b) ZEROe concept [6].   (c) N3-X concept [7].

Figure 1.1: Recent BWB concept aircraft.

No passenger plane has yet been manufactured with a BWB configuration. However, a partnership between NASA and Boeing designed a civil BWB aircraft — coined as X-48B — that made it to the air as a scaled model.

Ground vibration testing is essential during the airworthiness certification process of any aircraft since hardly ever do machines fail due to excessive strain [8]. Instead, they are much more prone to fail due to cracking caused by cyclical stress — fatigue. This phenomenon is actually responsible for more than 90% of the failures in Mechanical Engineering [9]. By providing experimental vibration data, validation and improvement of the structural dynamic models is made possible and these models can then be used to predict flutter behavior and plan flight tests.

In fact, GVT is performed in aircraft and their subcomponents to assess potential structural changes and damage. It usually calls for a significant number of high-performance accelerometers, which makes it a costly test to run.

1.3 Objectives and Deliverables

So that an aeroelastic analysis of the aircraft can be successfully performed, one must update its computational model in such a way that it mimics as accurately as possible the static and dynamic responses of the actual aircraft.

For the purpose of this thesis, GVT is to be conducted on the aircraft and computational tools are used in an attempt at describing its dynamic responses through a FEM. The focus here is on trying to optimize a simplified model made of beam elements and lumped masses instead of a complete FEM so that a study of how little freedom can be given to a model that still is able to correctly illustrate the reality can be performed.

During GVT, it is of extreme importance to accurately identify the first natural frequency happening on the aircraft's structures. This has to do with the fact that frequencies lower than the ones previously analytically predicted may compromise the behavior of the autopilot's filters.

As for the model updating, the frequency is to be matched in the first place. Once an optimized solution has been found for this, the study follows with the matching of mode shapes.

1.4 Thesis Outline

This thesis is divided into seven chapters, structured as follows:

- **Chapter 1: Introduction** introduces the objectives of the study presented in this thesis as well as the background leading to the work developed.

- **Chapter 2: Theoretical Background** details the fundamentals of Modal Analysis, Ground Vibration Testing and Model Updating.

- **Chapter 3: Beam Finite Element Model Update** comprises the study of updating the simplified model of a wing to match GVT data acquired from tests previously done at CfAR. Both frequency and mode shapes are attempted to be matched making use of *FEMtools* software.

- **Chapter 4: Experimental Testing and Data Post-Processing Procedures** covers the assumptions and the overall procedure to undergo during GVT on the aircraft, as well as methodology for extraction of the data. For that purpose a training test is performed on a wing structure specimen.

- **Chapter 5: Ground Vibration Testing** describes the two GVT test sessions on the aircraft, the post-processing of the extracted data and includes some comments on the results obtained.

- **Chapter 6: Aircraft Model Update** procedes with the model updating study of the assembled aircraft. Once more *FEMtools*' capabilities were used for matching frequencies. As for the mode shapes, an optimization algorithm was developed in *MATLAB*.

- **Chapter 7: Conclusions and Future Work** presents conclusions and states future work following this thesis.

Chapter 2

Theoretical Background

Dynamic aeroelasticity should be studied during the design and optimization phases for any aircraft. It dictates their performance and efficiency and consists in the interaction between three major forces: elastic, inertial and aerodynamic. This interaction between air loads, structural deformations and automatic flight control systems is more commonly experienced in contemporary aircraft, where flexible, light-weight structures, increased airspeeds and closed-loop automatic flight control systems all come together to create the most efficient vehicle [10].

This chapter provides some insights into fundamental topics on Modal Analysis theory, the main principles behind Ground Vibration Testing and an overview of the Model Updating process.

2.1   Modal Analysis

Having profoundly impacted both mechanical and aeronautical engineering over the last forty years, modal analysis has become a major technology when wanting to improve and optimize the dynamic characteristics of structures [11]. It can be described as being the process of exploring the inherent dynamic characteristics of a system in terms of its natural (or resonant) frequencies, damping factors and mode shapes with the main goal of formulating a mathematical model (coined as modal model) for studying its dynamic behavior.

When excited at one of its natural frequencies, any structure vibrates and deforms in what is called mode shape. In other words, the mode shape reflects the deformation caused by the vibration induced at that specific natural frequency. Under typical working conditions, a structure vibrates in a compounded combination of all mode shapes overlaid [12]. Nonetheless, the complete understanding of the potential ways a structure can vibrate is only acquired when one identifies every mode shape.

The quantification of natural frequencies, damping factors and mode shapes is possible through measurements of Frequency Response Functions (FRFs) during modal testing — which is an experimental technique to derive the modal model of a linear time-invariant vibratory system — at one location. By combining responses at different locations, a complete set of FRFs is obtained and that information is represented by a FRF matrix of the system [13].

5

Even though some degree of nonlinearity is always present in real Multiple Degree of Freedom (MDOF) structures, they can usually be approximated by the composition of Single Degree of Freedom (SDOF) linear models.

An important consideration to take into account during modal testing is how much FRF data is necessary to adequately describe the modal model of the system. These tests involve three main phases: test preparation — where the structure's support is selected as well as the type and location of excitation forces and the hardware to measure both forces and responses is chosen —, frequency response measurements and modal parameter identification.

As soon as the modal model is derived, one can instigate a plethora of applications. Among those, one has force identification, correlation analysis with Finite Element (FE) analysis, structural dynamic modification, active vibration control and one can even use it for troubleshooting purposes in order to gain some insight into a puzzling dynamic structure [14].

2.1.1 Eigenvalues and Eigenvectors

For the general damped case, the complete Newton's equation for a vibrating system with MDOFs can be modeled as a second order differential equation:

$$M\ddot{\boldsymbol{u}} + C\dot{\boldsymbol{u}} + K\boldsymbol{u} = \boldsymbol{f}, \tag{2.1}$$

where M, C and K are respectively the mass, damping and stiffness matrices and $\boldsymbol{u} = \boldsymbol{u}(t)$, $\dot{\boldsymbol{u}} = \dot{\boldsymbol{u}}(t)$ and $\ddot{\boldsymbol{u}} = \ddot{\boldsymbol{u}}(t)$ are the displacement, velocity and acceleration for each Degree of Freedom (DOF) of the modeled system. The equation adds up to the external excitation $\boldsymbol{f} = \boldsymbol{f}(t)$. By rewriting it in state space form one gets:

$$\begin{pmatrix} C & M \\ M & 0 \end{pmatrix} \begin{pmatrix} \dot{\boldsymbol{u}} \\ \ddot{\boldsymbol{u}} \end{pmatrix} + \begin{pmatrix} K & 0 \\ 0 & -M \end{pmatrix} \begin{pmatrix} \boldsymbol{u} \\ \dot{\boldsymbol{u}} \end{pmatrix} = \begin{pmatrix} \boldsymbol{f} \\ 0 \end{pmatrix}, \tag{2.2}$$

which can be further simplified as

$$A\dot{\boldsymbol{x}} + B\boldsymbol{x} = \widetilde{\boldsymbol{f}}, \tag{2.3}$$

where A, B, $\widetilde{\boldsymbol{f}}$, $\boldsymbol{x}$ and $\dot{\boldsymbol{x}}$ are:

$$A = \begin{pmatrix} C & M \\ M & 0 \end{pmatrix}, \tag{2.4}$$

$$B = \begin{pmatrix} K & 0 \\ 0 & -M \end{pmatrix}, \tag{2.5}$$

$$\widetilde{\boldsymbol{f}} = \begin{pmatrix} \boldsymbol{f} \\ 0 \end{pmatrix}, \tag{2.6}$$

6

$$\begin{cases} \boldsymbol{x} = \begin{pmatrix} \boldsymbol{u}^T & \dot{\boldsymbol{u}}^T \end{pmatrix}^T \\ \dot{\boldsymbol{x}} = \begin{pmatrix} \dot{\boldsymbol{u}}^T & \ddot{\boldsymbol{u}}^T \end{pmatrix}^T \end{cases} . \tag{2.7}$$

A first order ordinary differential equation can be recognized from (2.3) and a generalized family of solutions takes the following form

$$\boldsymbol{x} = \boldsymbol{\phi} e^{\omega t} = \begin{pmatrix} \phi \\ \lambda \phi \end{pmatrix} e^{\omega t}. \tag{2.8}$$

If (2.3) is set to equal 0, then the free vibrations of the system may be solved. The corresponding Laplace transform can be expressed as

$$|sA + B|X(s) = 0. \tag{2.9}$$

By multiplying this equation by A^{-1} on both members and making $\lambda = -s$, one can solve for the eigenvalues and eigenvectors. Since the coefficients of matrices A and B are real, the eigenvalues must be either real — for an overdamped system — or come in complex conjugate pairs — exhibiting free vibrations. For this reason, the latter is the one to focus on.

As poles come in complex conjugate pairs, by taking every second pole from the eigenvalues, one can write the poles with positive imaginary part as

$$s_i = -\zeta_i \omega_i + j \omega_i \sqrt{1 - \zeta_i^2} \tag{2.10}$$

for $i = 1, 2, 3, ..., N$. The complex conjugate poles s_i^* are obviously also poles of the system. In this equation ω_i represents the angular natural frequencies and ζ_i the damping. The relationship between the natural frequency, measured in Hertz, and the angular natural frequency can be expressed as

$$f_i = \frac{\omega_i}{2\pi}. \tag{2.11}$$

2.1.2 Frequency Response Function

For a linear system, a Transfer Function (TF) can be defined as the ratio between the Laplace Transform of the output $Y(s)$ and the Laplace Transform of the input $X(s)$:

$$H(s) = \frac{Y(s)}{X(s)} = \frac{\text{Laplace Transform of } y(t)}{\text{Laplace Transform of } x(t)}, \tag{2.12}$$

where, for instance, the Laplace Transform of $x(t)$, $X(s)$, is given for a continuous infinite length signal by

$$X(s) = \mathcal{L}\{x(t)\} = \int_0^{+\infty} x(t) e^{-st} dt. \tag{2.13}$$

The FRF, $H(f)$, is the ratio between the Fourier Transform of the output signal $Y(f)$ and the Fourier

Transform of the input signal $X(f)$. This occurs in the frequency domain and the FRF is an entity that can be experimentally measured, whereas the TF is a mathematical abstract entity that can be used as a tool for solving differential equations.

Fig.2.1 depicts the correspondence between representations of time and frequency domains for the same signals.
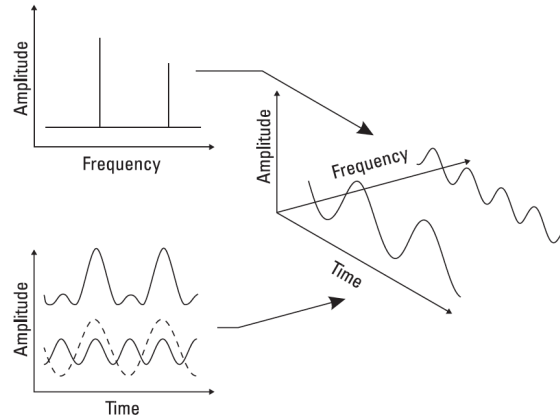
Figure 2.1: Relationship between time and frequency domains [15].

The FRF is obtained by evaluating the TF on the imaginary axis in the Laplace domain where $s = i\omega$. For a MDOF system, the FRF contains all the receptance frequency responses for that system. As previously mentioned, measurements are sampled in the time domain — such as acceleration and force — which may then be transformed into the frequency domain using the Fourier Transform, usually making use of a discrete variation of the Fourier Transform, known as Fast Fourier Transform (FFT) method.

Any FRF can be represented in terms of amplitude and phase or in terms of real and imaginary parts, usually using Bode Diagrams. Examples of this can be seen in Fig.2.2 and the way to relate both kinds of representation makes use of the formulas

$$\text{Amplitude} = \sqrt{\text{Re}^2 + \text{Im}^2} \tag{2.14}$$

and

$$\text{Phase} = \arctan\left(\frac{\text{Im}}{\text{Re}}\right). \tag{2.15}$$

The amplitude represents the ratio between the input force and the response and can be expressed, for example, in g/N while the phases diagram comes expressed in degrees and gives information on whether the motion of the structure is happening in or out of phase with the input.

As previously mentioned, including sufficient points while testing is of extreme importance to thoroughly describe the modes of interest. It is also known that a mode of vibration can be excited at any point of the structure as long as not in a nodal point — where there is no motion [17]. The frequency and damping of a mode can therefore be extracted from measurements such as the ones in Fig.2.3, given

8
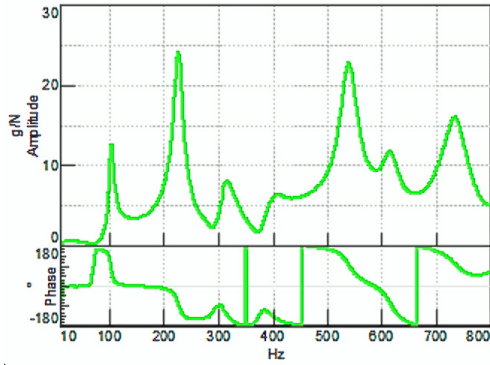
(a) FRF expressed in terms of Amplitude and Phase.
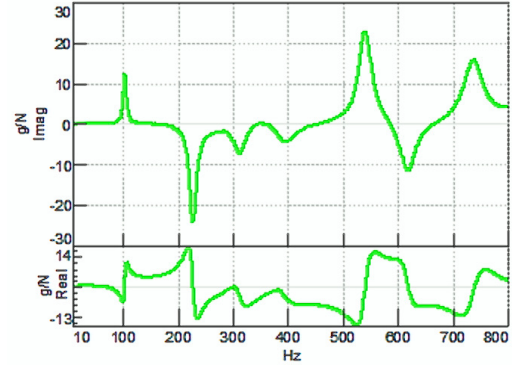
(b) FRF expressed in terms of Real and Imaginary parts.

Figure 2.2: Bode diagrams for FRF [16].

that both frequency and damping of any mode are global properties of the structure. The real part of a FRF equals zero at resonant frequencies and the imaginary part presents peaks either above or below zero at these same frequencies. Hence, by acquiring FRFs at different locations on the structure, one can use their imaginary part to plot the mode shapes by taking into account the direction and intensity of the peaks.
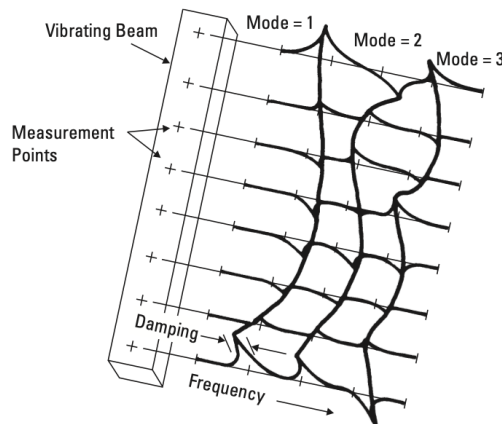
Figure 2.3: Method for extraction of mode shapes. Damping and frequency — same at each measurement point. Mode shape — obtained at constant frequency from all measurement points [17].

The natural frequencies are then identified by the peaks appearing at the same frequency at every measurement point and these amplitudes combined describe the mode shape for the corresponding natural frequency. The damping, on the other hand, can be determined by the half-power method, which quantifies the sharpness of each resonant peak [18]. To do so, points surrounding the magnitude peak of the FRF that are 3 dB down from the peak value — which correspond to the points where the amplitude is 0.7071 times the resonant one — are identified. These are called half-power points and the wider the peak is, the higher the damping [12].

If f_i is the natural frequency for mode i and Δf_i is the frequency bandwidth between two half-power points (one bellow and the other above the resonant frequency) for that same frequency, then one can compute the damping ratio for frequency i, ζ_i, as

9

$$\zeta_i = \frac{\Delta f_i}{2 f_i}.$$

(2.16)

For determining the mode shapes, one makes use of the quadrature picking technique, which assumes light coupling between the modes [19]. When this happens, the structural response at a given resonant frequency is dominated by that mode and therefore quadrature picking can be used to unravel the mode shapes. As depicted in Fig.2.3, for SDOF systems, the FRF at natural frequencies is purely imaginary and consequently, the value of the imaginary part is proportional to the modal displacement. As will later be explained, by examining it at a number of points on the structure, the modal relative displacement at each point is found.

2.2 Ground Vibration Tests

Testing is a powerful tool for the certification process and Ground Vibration Testing is one of the means of compliance during verification tasks. Usually happening right before the first flight, this test is performed at the integrated aircraft level and conducted to fulfill requirements imposed by certification authorities such as the certification specification for normal, utility, aerobatic and commuter aircraft CS23.629 [20] — which defines the critical requirements for which the aircraft is free from flutter, divergence and control reversal at any condition of operation within the flight envelope — and the similar one but for larger aircraft CS25.629 [21].

Thus, this large-scale modal test on the full aircraft serves the purpose of calibrating FEMs used for further flutter predictions. Additionally, structural coupling tests and control laws are typically performed simultaneously to help calibrate the simulation models [4].

Test preparation as well as post-test analysis can be accelerated with the integrated use of FEMs. Properly choosing both the data acquisition system and excitation techniques also play an important role when worried about the efficiency of the test. The answer to questions like 'how many accelerometers should be used?', 'where should they be placed on the structure?', 'how should the aircraft be supported to simulate a free-free condition and so that the first flexible mode is well separated from the rigid body modes?' needs to be well established before moving to the testing phase and using computer-based FEMs is crucial when the availability of the aircraft is limited.

2.2.1 Data Acquisition

The first step in modal analysis experiments is measuring both the excitation (input) and responses (output) of the structure being tested. The structure is to be excited and the applied excitation force, as well as the resulting response vibrations — typically accelerations — are measured, resulting in a FRF data set. This collected data is then used to identify the modal parameters such as the natural frequencies, damping factors and mode shapes — which can then be visually animated.

The Data Acquisition System (DAS) used for GVT in this thesis is a National Instruments NI cDAQ-9188, making use of IEPE NI 9234 acquisition cards. With the resources available, one was able to use

up to 21 channels simultaneously, meaning one hammer and up to 20 sensors at the same time.

Conversion and amplification of analogue signals into digital ones is accomplished by LabView software, which stores a data block for each DOF by computing the FRF matrix for multiple input multiple output systems based on a built-in FFT algorithm.

2.2.2 Shaker Testing vs. Impact Testing

When deciding how to excite a structure and what the excitation function that best suits the application is, one has to evaluate both pros and cons of each of the possibilities available to date whilst taking into account they are interrelated.

The excitation function is the mathematical signal used as input and the excitation system is the physical mechanism employed to transmit the signal. Generally speaking, the choosing of the excitation function dictates the choice of the excitation system and the reverse is also true. For example, a true random or burst random function requires the use of a shaker for implementation and the choosing of a hammer implies an impulsive type excitation function.

In terms of excitation functions, these fall into four main categories: steady-state, random, periodic and transient [17]. True random, burst random and impulse types are the most useful for modal testing and also the most widely implemented.

With regards to excitation mechanisms, these can also fall into four categories: shaker, impactor, step relaxation and self-operating. For the purpose of this thesis, only shaker and impact testing will be discussed, since they are the methodologies that are associated to the desired excitation functions.

The most commonly used shakers for modal analysis are electromagnetic (as shown in Fig.2.4) and the electro-hydraulic ones. For the electromagnetic, force is generated by an alternating current driving a magnetic coil. The maximum frequency limit can vary from 5 kHz to 20 kHz and maximum force rating from 9 N to 4450 N, depending on the size of the shaker itself.
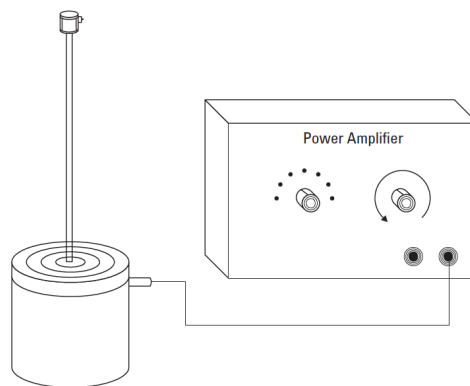
Figure 2.4: Electrodynamic shaker with power amplifier and signal source [17].

The major drawbacks associated with the use of shakers for modal testing include:

- The change in the dynamics of the structure produced by the shaker, which is physically mounted to the structure via the force transducer.

- In practical scenarios, when a structure is displaced along a linear axis there is also tendency for it to rotate about the other two axes. This problem of forces being applied in other directions can be minimized by connecting the shaker to the load cell through a slender rod — called a stringer — that allows the structure to move freely in the other directions.

- The reaction forces that can be transmitted through the base of the shaker back to the structure whenever the main body of the shaker is not well isolated from the structure.

- In electromagnetic shakers, the mismatch in the impedance that can exist between the structure and the shaker coil. At resonance with small effective mass, little force is required to produce a response, which can result in a drop in the force spectrum in the vicinity of the resonance, causing the force measurement to be susceptible to noise.

An impact device such as an impact hammer (such as the one represented in Fig.2.5) is another typical excitation mechanism. Providing shorter measurement times and requiring little hardware, it is a relatively simple technique to be implemented. Nonetheless, it is difficult to obtain consistent results with it and special attention to some details needs to be taken.
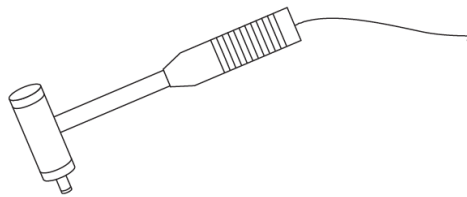
Figure 2.5: Impact hammer [17].

Since the force to be applied by an impact hammer is an impulse, the amplitude level of the energy to be applied to the structure depends on its linear momentum — for which contribute the mass and velocity of the hammer. The hammer's velocity is difficult to control, so the force level is usually controlled by varying the mass instead. Impact hammers are therefore available in varying weights and mass can also be added to or removed from the majority of hammers, making them useful for testing on a different range of objects of different sizes and weights.

The frequency content of the energy applied to the structure is a function of the stiffness of the contacting surfaces and the stiffness of these affects the shape of the force pulse thus determining the frequency content. Since it is not feasible to change the stiffness of the structure being tested, the stiffness of the hammer tip is what is chosen to vary. The harder the tip is, the shorter the duration of the pulse will be and consequently the higher the frequency content. This can be observed in Fig.2.6.

Among the disadvantages of the use of impact hammers on modal testing one has:

- Noise and leakage, which can be present in a response signal as a result of a long time record or a short time record respectively. This problem can be tackled with proper windowing techniques.

- The fact that less control over the inputs is attained using an impact hammer in comparison with a shaker.
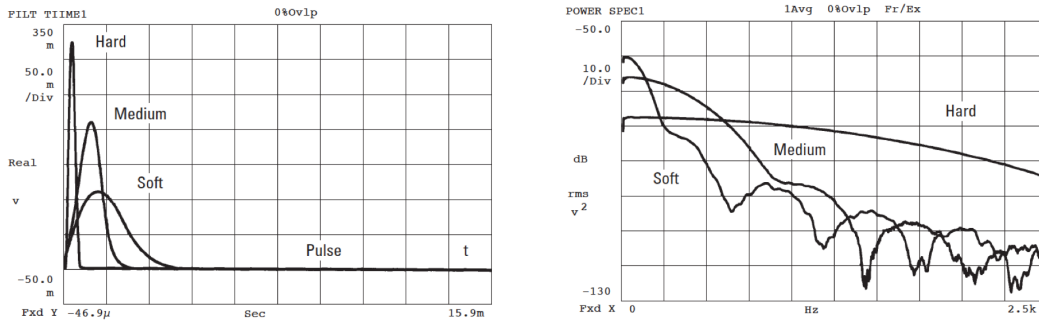
Figure 2.6: Frequency content for various pulses [17].

- The fact that the duration of the contact time during the impact influences the frequency content of the force, with a longer contact time meaning a smaller range of bandwidth.

- The difficulty to excite structures with complex geometries.

Shakers not only allow more control over the excitation force — including its type, amplitude, phase and frequency range — but also sample more information than the hammer per unit of time, since they are able to apply more energy to the structure for longer. On the other hand, the fact that no mass is attached nor extra stiffness applied to the structure is a clear advantage of the impact hammer. Even though the hammer is a more expedite alternative, both methods share the fact that the setup time takes longer than the test time itself.

Due to the equipment already available at CfAR and expensive costs associated with buying or renting a modal shaker, the methodology chosen for performing GVT was the one using an impact hammer. The DOFs in impact hammer testing correspond to places marked along a structure where data is collected. For the purpose of collecting accelerations, two different factors have to be taken into account when performing GVT if one is concerned with the mode shape extraction.

Firstly, if one decides to rove the sensors, the sensors have to be placed in points of the structure that do not correspond to nodes of the mode shapes one is interested in observing. If on the other hand, the hammer is to be roved, then the DOFs chosen to tap the hammer on have to not coincide with the location of the nodes. Further details on the differences between roving the accelerometers and roving the hammer — as well as which one is the most adequate in this situation — will be given in the following section.

Nodes are points corresponding to no displacement of the structures to be studied while anti-nodes correspond to the points of maximum displacement during each vibration cycle.

Secondly, the number of DOFs chosen to extract FRFs for each structure has to be enough so that aliasing does not happen. Aliasing is a phenomenon happening when one samples, for example, a sine signal with a sampling frequency less than twice the frequency of the sine, resulting in a sine signal of a different frequency [22].

Given the reasons stated above, it is obvious the need for careful selection of sensor placement or hammer taps and that can be eased by previously analyzing the FEM of the aircraft.

13

Roving Accelerometer vs. Roving Hammer

When chosen to perform a modal test with an impact hammer on a structure without as many sensors (accelerometers) as the desired number of DOFs, one has to decide whether to rove the accelerometers or to rove the hammer.

From a theoretical standpoint there is reciprocity when using any of the two techniques so the choice usually leans towards the roving hammer technique for practicality reasons.

As the name suggests, the roving accelerometer technique implies moving the accelerometer while the excitation source remains at the same point, meaning that the sensor is to be moved to the points where a FRF is to be measured. The roving hammer technique, on the contrary, implies the fixing of the sensor at a certain point and the excitation source to move from DOF to DOF in which the FRF is to be measured. Both methods are conceptually displayed in Fig.2.7.

(a) Roving accelerometer method.　　　　(b) Roving hammer method.
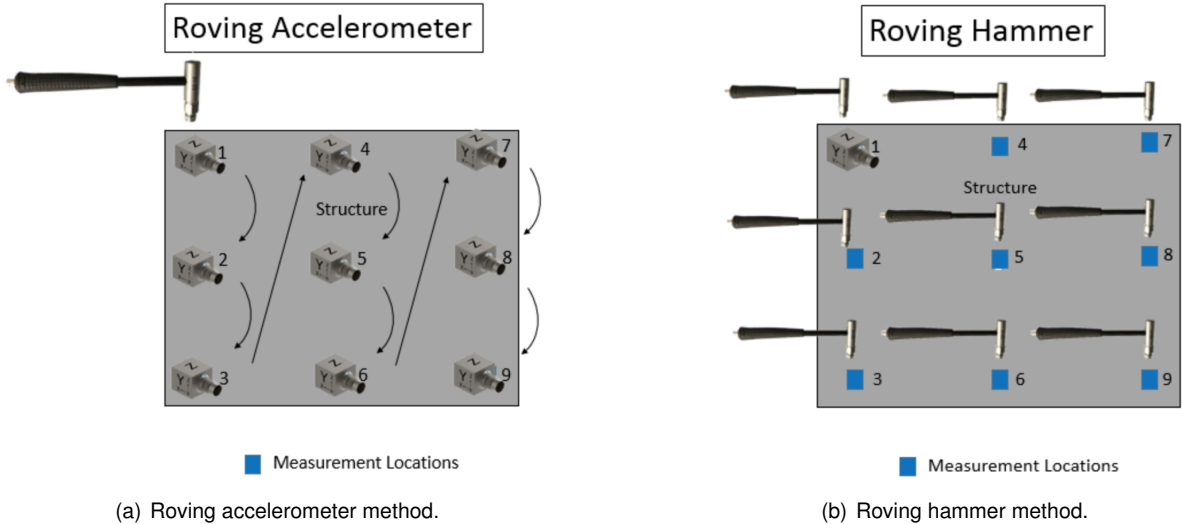
Figure 2.7: Comparison between roving accelerometer and roving hammer methods [23].

Whilst roving the hammer can be logistically simpler, it can require much more data extractions when the accelerometers measure triaxial accelerations. For the purpose of GVT on this aircraft, the question of whether it should or should not be considered to rove the accelerometers does not arise since the accelerometers to be used are uniaxial. Instead, the need to unmount and remount them over all the DOFs would be a major drawback and would take much longer. Another disadvantage of moving the sensors is the effect the mass loading could have when gluing the sensors on all the different locations throughout the structures of the aircraft.

For these reasons, given the equivalence between both methodologies from a physics point of view, roving the hammer was chosen as the technique to go for during the testing of this aircraft.

2.3 Finite Element Model Updating

The purpose of model updating is to study how changes in a structure's design influence its response. That is usually achieved by minimizing an error function that evaluates the deviation between analytic and experimental data.

A FEM is only reliable when experimental data corroborates and validates it. Moreover, for flutter analysis on an aircraft, a simplified model has to accurately represent the physical structures under study. That being the case, the model updating process ensures problems such as manufacturing weight differences, flawed boundary conditions definition and incorrect assumptions on properties of the materials are reckoned. Fig.2.8 schematizes the FEM updating iterative process.
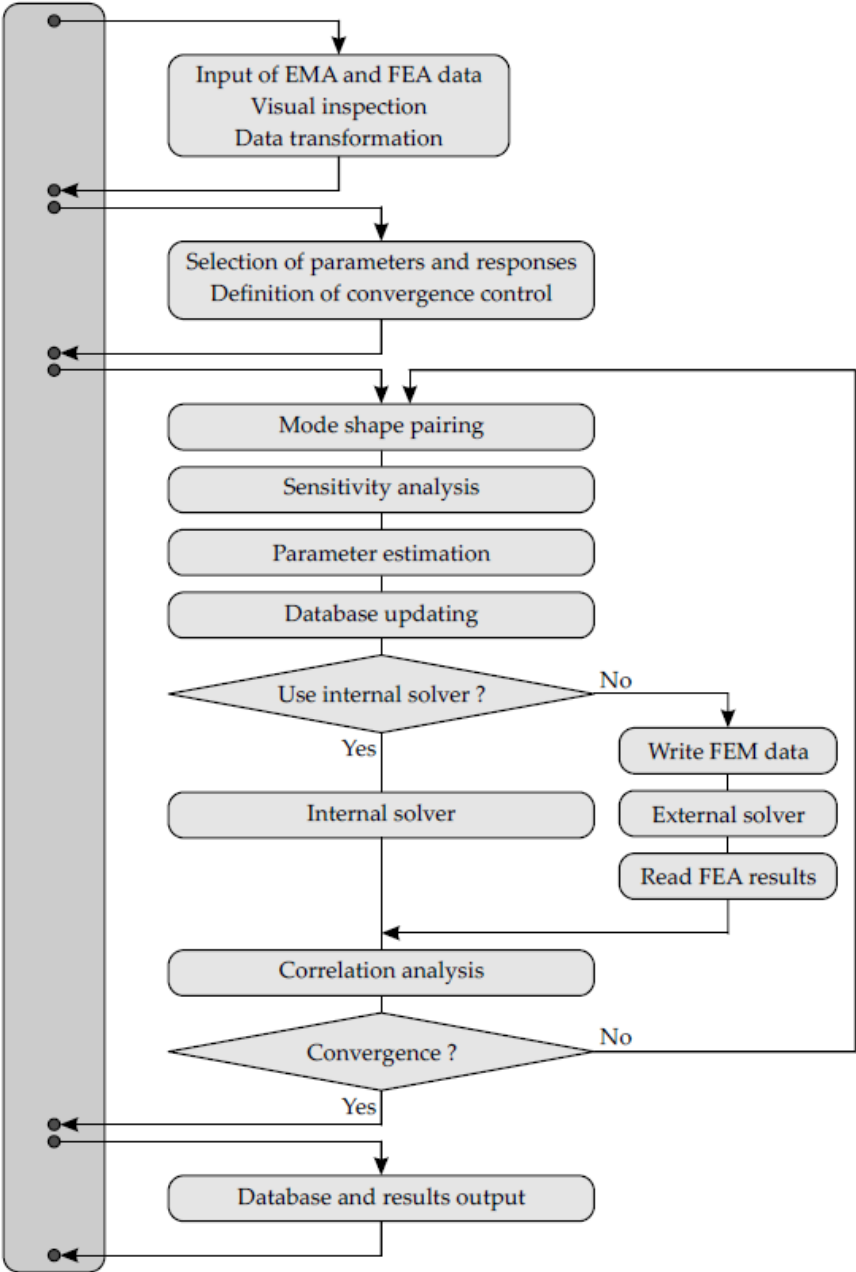
Figure 2.8: Model updating iterative loop [24].

The software used to explore the model updating process in this thesis was initially *FEMtools*. While in the loop shown in the figure, modal analysis is performed through *Ansys APDL* instead of *FEMtools*' internal solver.

For mode shape model updating of the aircraft in which GVT was performed, a different approach making use of an optimization algorithm in *MATLAB* was also used. Its formulation will be explained in Chapter 6.

2.3.1 Modal Assurance Criterion

As a good statistic indicator for how consistent modes shapes are between themselves, one has the Modal Assurance Criterion (MAC), bounded between 0 — indicating inconsistency — and 1 — indicating fully consistent mode shapes — which is frequently used to evaluate and compare mode shapes obtained experimentally with the ones derived from analytical models [25]. It measures the squared cosine of the angle between two mode shapes and mathematically one has

$$\text{MAC}(\psi_a, \psi_e) = \frac{\left|\{\psi_a\}^T\{\psi_e\}\right|^2}{\left(\{\psi_a\}^T\{\psi_a\}\right)\left(\{\psi_e\}^T\{\psi_e\}\right)}, \tag{2.17}$$

where ψ_a is the analytical modal vector and ψ_e is the experimental modal vector.

These days, the most frequent way to present MAC information is through either a 2D or 3D plot as the examples shown in Fig.2.9, where discrete mode to mode comparison is represented. It should be noted that, despite being a great tool as an assurance indicator, it can only indicate consistency, not validity nor orthogonality [26]. Therefore, attention should be paid while making use of this criterion and some misuses should be addressed.

(a) 2D presentation of MAC values.   (b) 3D presentation of MAC values.
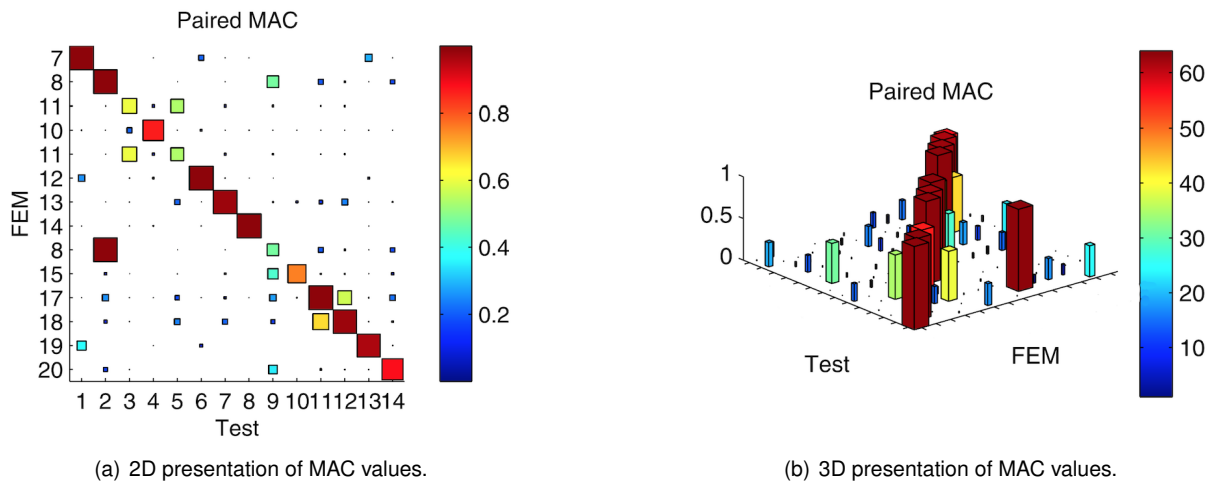
Figure 2.9: Examples of modes of presenting MAC values [27].

Generally speaking, the MAC can assume values close to zero, representing that the modal vectors are not consistent, when:

• The system is nonstationary, which can occur if the system changes mass, stiffness or damping

during testing. When the system is nonlinear and two data sets have been collected at different time or excitation levels, they may appear different in FRFs generated from different excitation signals and the modal parameters estimation algorithm will not be able to handle nonlinear characteristics in a consistent fashion.

- There is significant noise on the reference mode shape and no amount of signal processing is capable of removing this type of error.

- The modal vectors are from linearly unrelated mode shape vectors. However, this measure of inconsistency implies that the modal vectors are orthogonal since the estimates are from different excitation positions.

On the other hand, values closer to unity may be obtained, meaning consistency between the modal vectors but not necessarily representing correctness, in situations where:

- The number of DOFs is not sufficient to distinguish between independent mode shapes, which may occur when too few response stations have been used in the experimental determination of the modal vector, leading to an incompletely measured modal vector. Since the the FEM generally contains more DOFs than the experimental model, the analytical normal modes can be truncated to eliminate data to which there is no counterpart to [24]. This process can compromise the correlation analysis of modes, making it impossible to distinguish between different mode shapes. This effect is called spatial aliasing and Fig. 2.10 schematizes the mechanism of truncation for MAC computation.
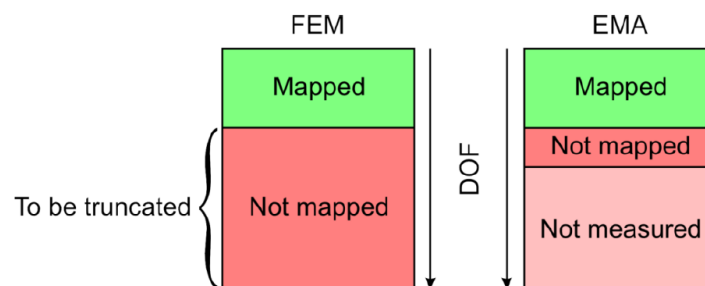
Figure 2.10: Mode shape truncation [24].

- The modal vectors are the result of a forced excitation other than the desired input, which can happen when, for example, a rotating piece of equipment with an unbalance is present in the system being tested, resulting in the wrong measurement of the FRF.

- The mode shapes are predominantly coherent noise, being simply a random noise vector or a vector reflecting the bias in the modal parameter estimation algorithm.

- The modal vectors represent the same modal vector but with different scaling. The MAC measures the mode shapes without reference to the scaling of each modal vector, meaning that a mode shape with more influence on the overall response of the FEM may not have the same influence

17

on the response of the experimental model. This makes MAC easy to use, since there is no need to determine modal masses to compute it but also limits its applicability (given that two mode shapes can be very correlated and yet different in terms of scale) [27].

For the purpose of this thesis, values of MAC above 0.9 will be considered as well correlated while values bellow 0.6 should be considered with caution because they may or may not indicate correlation and therefore lack of resemblance.

2.3.2 Correlation Coefficients

Several Correlation Coefficients (CCs) can be chosen to be minimized during the FEM updating. *FEM-tools* software allows one to choose from a range of CCs, stated bellow [24]:

- CCMEAN measures the weighted relative difference between resonance frequencies:

$$ \text{CCMEAN} = \frac{1}{C_R} \sum_{i=1}^{N} C_{R_i} \frac{\Delta f_i}{f_i}, \tag{2.18} $$

with $C_R = \sum_{i=1}^{N} C_{R_i}$, where C_{R_i} are the weighted response confidences of the various responses and Δ representing the difference between the experimental and the analytical physical quantity.

- CCABS measures the weighted absolute relative difference between resonance frequencies:

$$ \text{CCABS} = \frac{1}{C_R} \sum_{i=1}^{N} C_{R_i} \frac{|\Delta f_i|}{f_i}. \tag{2.19} $$

- CCDISP is a measure of the weighted absolute relative difference between displacements:

$$ \text{CCDISP} = \frac{1}{C_R} \sum_{i=1}^{N} C_{R_i} \frac{|\Delta \psi_i|}{\psi_i}. \tag{2.20} $$

- CCMASS is the weighted absolute relative difference between exact mass and the calculated one:

$$ \text{CCMASS} = \frac{1}{C_R} \sum_{i=1}^{N} C_{R_i} \frac{|\Delta m_i|}{m_i}. \tag{2.21} $$

- CCMAC measures the weighted difference between target and average actual MAC:

$$ \text{CCMAC} = 1 - \frac{1}{C_R} \sum_{i=1}^{N} C_{R_i} \text{MAC}_i, \tag{2.22} $$

with N being the number of active MAC responses.

- CCTOTAL is the total CC value, which accounts for all of the four last stated ones:

$$ \text{CCTOTAL} = \text{CCABS} + \text{CCDISP} + \text{CCMASS} + \text{CCMAC}. \tag{2.23} $$

2.3.3 Convergence Criteria

FEMtools uses the CCs as objective functions that need to be minimized. When performing a new iteration, it automatically verifies the values of the CC and checks if a convergence criterion has been satisfied. The iteration loop in model updating will stop as soon as one of the following tests is satisfied [24]:

- The value of the reference CC is lower than an imposed margin ε_1 at iteration t:

$$\mathrm{CC}_t < \varepsilon_1, \tag{2.24}$$

  where CC_t is the reference CC at iteration t.

- Two consecutive values of the reference CC are within a chosen margin ε_2:

$$|\mathrm{CC}_{t+1} - \mathrm{CC}_t| < \varepsilon_2. \tag{2.25}$$

- The number of iterations exceeds the value initially allowed, setting a practical limit for situations in which significantly small convergence margins are used.

For this thesis purpose, the most important CCs to be used when model updating are CCABS when focused on the convergence of modal frequencies and CCTOTAL when a broader convergence is the preferable option.

Chapter 3

Beam Finite Element Model Update

FEMs are considered one of the foremost tools for structural analysis. As a preparation for what will later be the model updating phase for the obtained GVT results for the BWB aircraft, this chapter will review an attempt at model updating the results previously obtained at CfAR by another student.

The choice of doing so not only made the process of model updating much more clear and expedite but also took advantage of the fact that the time frame to perform the GVT was not going to be allocated right at the beginning of this thesis study.

3.1 Previously Obtained GVT Results

During his masters thesis at CfAR, Araújo [3] had the opportunity of performing the GVT for the right wing of the Bombardier BWB before it was assembled. The results he obtained for the natural frequencies can be observed in Table 3.1 and the mode shapes associated with these resonant frequencies can be seen in Fig.3.1 by ascending order from (a) to (g).

Table 3.1: Natural frequencies obtained by Araújo during GVT on the wing.

Mode #	f_{EMA} (Hz)
1	10.34
2	35.28
3	50.38
4	81.34
5	129.80
6	142.72
7	157.48

After the test phase, an attempt at model updating based on frequencies and mode shapes was made. For that purpose, Araújo developed a simplified FEM as being a beam element model with rectangular cross sections connecting the centroid of 50 wingbox sections along the span of the wing.

The boundary condition was chosen to best simulate experimental conditions, meaning that the root of the wing was fixed at all 6 of its DOFs — 3 for translation and 3 for rotation. With respect to values for

(a) 1st out-of-plane bending — side view.

(b) 2nd out-of-plane bending — side view.

(c) 1st in-plane bending — top view.

(d) 3rd out-of-plane bending — side view.

(e) 2nd in-plane bending — top view.

(f) 1st out-of-plane torsion — top view.

(g) Not identified — top view.
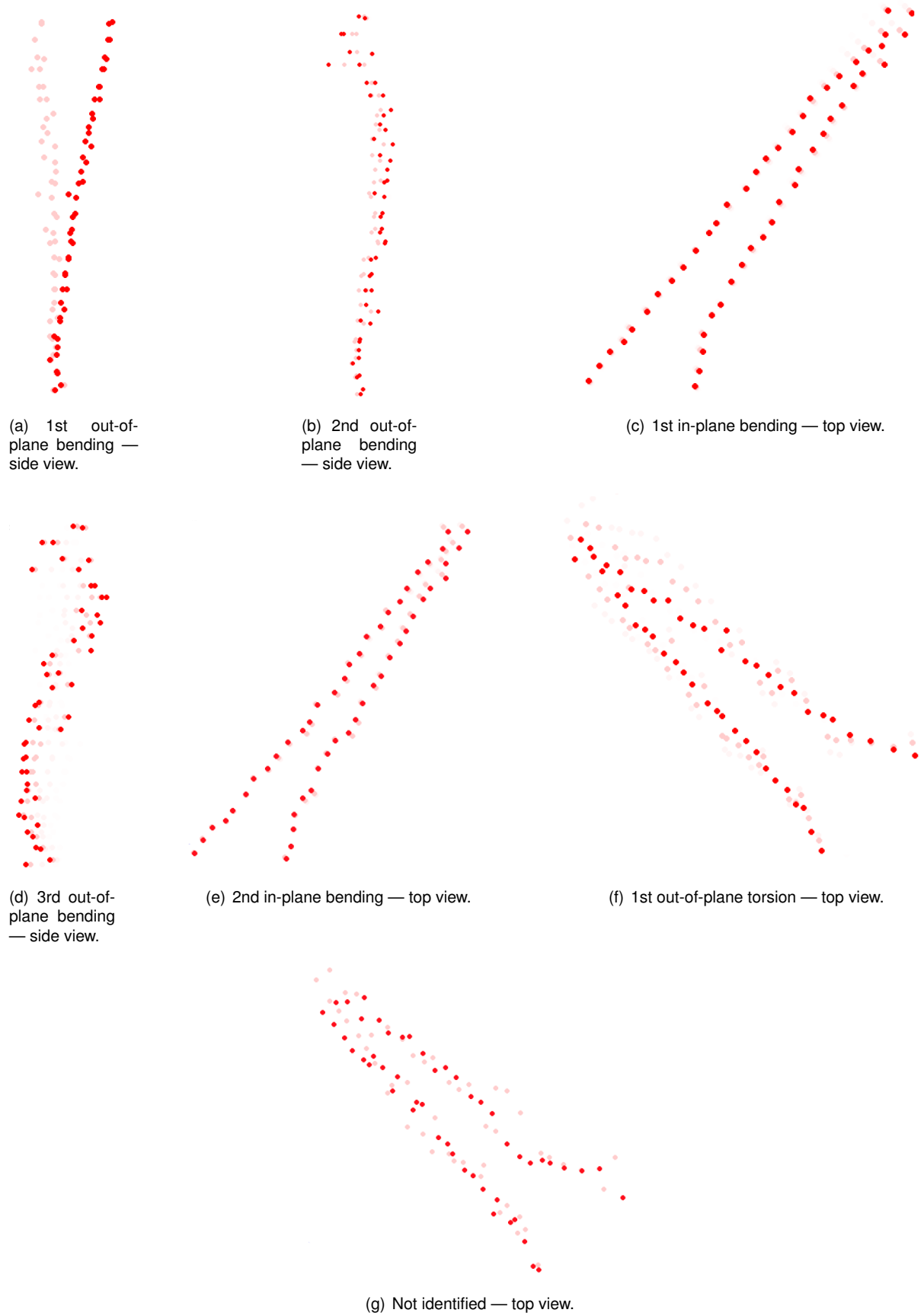
Figure 3.1: Experimental mode shapes obtained by Araújo for the right wing.

Young's modulus and mass density, these were defined based on the properties of the material used for most of the wing.

At the end of his thesis, the matching of the frequencies was successfully obtained but when trying to match mode shapes no convergence was reached. The reason for this may have to do with the need for higher FEM complexity, so the next step was considered to be creating a simple enough model for reasonable computational times but with more freedom to change parameters when model updating.

3.2   Beam Model

The higher complexity FEM was developed using *Ansys Mechanical APDL* capabilities. After several iterations, the chosen model is the one presented in Fig.3.2. It features element types BEAM188 for the beams (24 along the central spine of the model and 25 transverse ones on each side) and MASS21 for each of for the mass points located at the junction and at the end of the beams, corresponding to a total of 74 beam elements and 75 lumped masses.
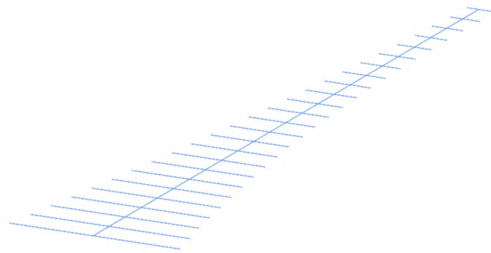
Figure 3.2: FEM developed in Ansys Mechanical APDL.

The root of the wing was once again fixed for all DOFs in order to simulate the conditions in which the tests had been performed. The results obtained for the natural frequencies of the FEM from *Ansys* are shown in Table 3.2. In this table one can see once more the natural frequencies obtained experimentally by Araújo and the relative difference between the corresponding mode shapes obtained through experimental and computational methods before any model updating iteration.

Table 3.2: Initial natural frequencies for the FEM and comparison with experimental ones.

Mode #	f_{EMA} (Hz)	f_{FEA} (Hz)	Δ_f (%)
1	10.34	4.11	-60.23
2	35.28	22.92	-35.03
3	50.38	29.90	-40.65
4	81.34	61.95	-23.84
5	129.80	120.09	-7.48
6	142.72	165.63	16.05
7	157.48	196.95	25.06

3.3 FEMtools Model Updating

The software used for the model updating was *FEMtools*. The procedure to be followed starts with the node pairing between the DOFs for which data was obtained during the experimental results — Fig.3.3(a) — with the closest mass point of the developed FEM — Fig.3.3(b).

(a) Spatial disposition of DOFs for GVT performed by Araújo [3] on wing.

(b) Matching between experimental DOFs with closest mass points on the FEM.
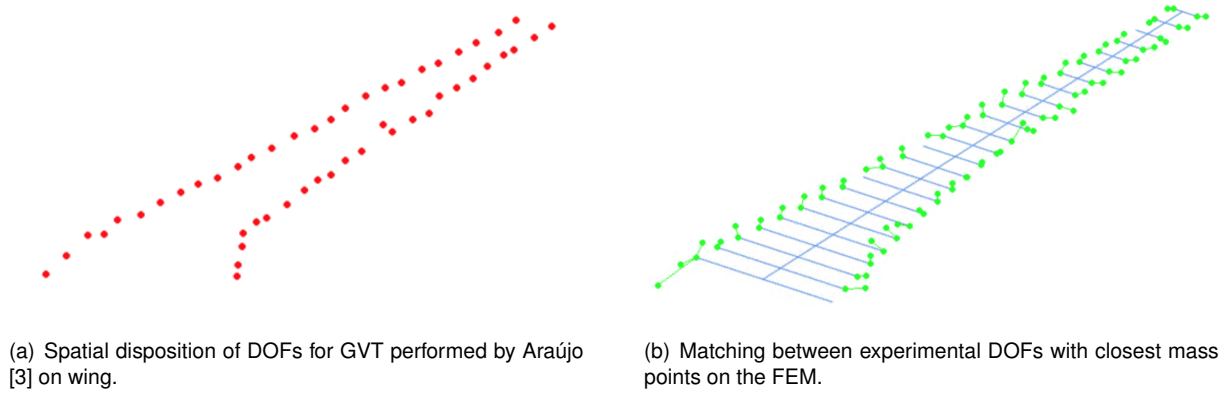
Figure 3.3: FEMtools display of experimental DOFs and node-point pairing between models.

The stiffness and mass matrices can be simultaneously computed for the FEM and the response type should be set to 'Modal Responses'. A mode shape pair is to be defined on the following step so that the software knows which frequencies or mode shapes it should try to match. After that, correlation coefficients are computed by *FEMtools* and the structural parameters one allows to change have to be selected. As for this thesis study, the parameters were chosen to be the ones presented in Table 3.3. Since the goal here is trying to find how little freedom one can give the model for it to accurately match the experiments, the combinations of parameters vary from iteration to iteration but only combinations of parameters from this set were considered.

Table 3.3: Structural parameters to change during model update.

Parameter	Description
E	Young's modulus
ρ	Mass density
A	Cross section area
I_x	Torsional stiffness
I_y	Bending moment of inertial about y
I_z	Bending moment of inertial about z
m_G	Lumped mass

Having chosen the cross section of the beam elements to be rectangular, the cross section second moments of area can therefore be simply given by the product of the base b and height h of the rectangle:

$$A = b \cdot h. \tag{3.1}$$

The choosing of these parameters has implications in the values for the bending moments of inertia

I_y and I_z. For this reason, the ration b/h was selected so that the ratio I_y/I_z obtained from the complete FEM developed at CfAR for the wing was ensured. This relationship can be expressed by:

$$\frac{I_y}{I_z} = \frac{\frac{1}{12}bh^3}{\frac{1}{12}b^3h} = \left(\frac{b}{h}\right)^{-2}.$$ (3.2)

Being also studied in this chapter, the torsional stiffness I_x is given by the sum of the two moments described above:

$$I_x = I_y + I_z.$$ (3.3)

3.3.1 Updating Based on Frequencies

On a first approach, all the mode shapes collected from the experiments were selected to be matched to the corresponding mode shape extracted from *Ansys*. This means that the software is set to try to update the computational values of the resonant frequencies, f_{FEA}, with the values of f_{EMA} on a sequential order.

Since the focus at this point relies on the frequencies and not on the mode shapes, the CC to be concerned with is the CCABS. Hence the choosing of this one to be the convergence control setting for the study presented next. As for the convergence criteria, the margin ε_1 was selected to be 1 and the margin ε_2 was chosen as 0.1. The maximum number of iterations the software was allowed to performed was also set to 50, in case none of the previous two criteria was reached.

Model update of E

On a first attempt at reaching the lowest possible value for CCABS, the Young's modulus was chosen to be updated alone. Adding to a total of 74 Design Variables (DVs), the model update process took 29 iterations until one of the convergence criteria was reached. Nonetheless, the one to be reached was the one which evaluates the difference between two consecutive iterations — equation (2.25).

In fact the CCABS, initially at 29.5%, converged to 16.7% after the 29th iteration. This value, despite being approximately half the initial one, is still unsatisfactory. The results obtained are shown in Table 3.4, along with the relative error obtained for the different mode shape pairs.

Table 3.4: Results obtained for model updating of E.

Mode #	f_{EMA} (Hz)	f_{FEA_E} (Hz)	Δ_{f_E} (%)
1	10.34	10.18	-1.54
2	35.28	28.44	-19.39
3	50.38	70.84	40.61
4	81.34	74.22	-8.75
5	129.80	110.26	-15.05
6	142.72	142.67	-0.04
7	157.48	207.40	31.70

Following model updates

Based on the previously obtained results, different choices of parameters to change were selected. The combinations were the following:

- Updating of E and ρ.

- Updating of E, ρ and m_G.

- Updating of E, ρ, A and m_G.

- Updating of E, ρ, A, I_x, I_y, I_z and m_G.

Once again, the results obtained reflect the attempts at matching frequencies. These can be seen in Table 3.5.

Table 3.5: Results obtained for the succeeding model updates.

Mode #	f_{EMA} (Hz)	$f_{\text{FEA}_{E,\rho}}$ (Hz)	$f_{\text{FEA}_{E,\rho,m_G}}$ (Hz)	$f_{\text{FEA}_{E,\rho,A,m_G}}$ (Hz)	$f_{\text{FEA}_{E,\rho,A,I_x,I_y,I_z,m_G}}$ (Hz)
1	10.34	8.52	8.44	8.63	10.29
2	35.28	28.11	28.00	35.27	35.04
3	50.38	62.14	61.58	62.92	50.27
4	81.34	78.32	77.72	81.36	80.70
5	129.80	120.18	119.55	129.93	128.58
6	142.72	153.82	154.86	142.93	142.87
7	157.48	204.95	204.26	157.61	160.36

For each of the selection of parameters to be updated, the number of DVs, number of iterations until convergence and final value for CCABS are presented in Table 3.6.

Table 3.6: Comparison of convergence related data between different model updates.

Update of	# DVs	# Iterations	CCABS$_{\text{final}}$ (%)
E	74	29	16.7
E, ρ	223	9	15.8
E, ρ, m_G	298	7	16.0
E, ρ, A, m_G	372	17	6.0
$E, \rho, A, I_x, I_y, I_z, m_G$	594	4	0.72

One interesting result to be discussed is the introduction of m_G. Even though the number of DVs grew by 25%, the final CCABS evaluated at the end of the last iteration was higher than the one where only E and ρ were chosen to update. However, this happened at a lower overall number of iterations, meaning that the global number of parameter updates performed by *FEMtools* was lower for the case where m_G was introduced, hence the higher CCABS$_{\text{final}}$.

As a way of comparing the obtained results, the relative difference between experimental and computational data is plotted for every mode shape pair in Fig.3.4. One can then infer that the most difficult resonant frequencies to be matched were the ones corresponding to the 3rd and 7th mode shapes.
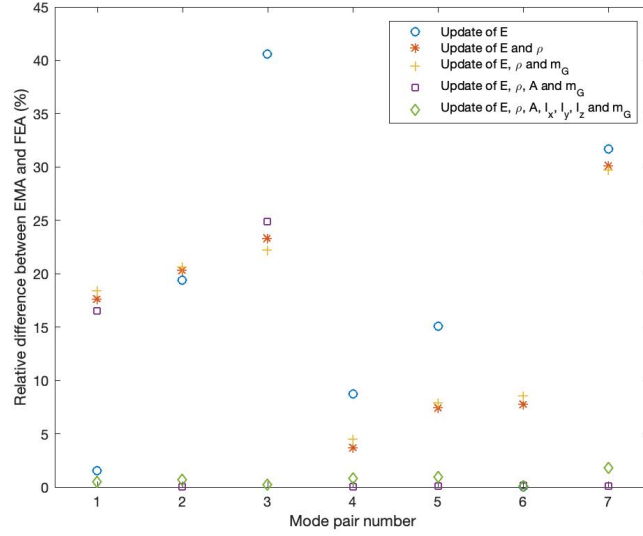
Figure 3.4: Relative error for mode shape pairs in the different model updates.

Having as a goal reaching a value for CCABS$_{final}$ lower than 1, the update of all the structural parameters in the last try presented was considered to be enough. That being said, it is probably not the most efficient way of doing so given the large number of DVs. As a last step before proceeding to the model update based on the obtained mode shapes, an update of a lower number of DVs is attempted, taking into account the results obtained so far.

Both m_G and I_x were not considered for this final try given the low impact they are predicted to have on the final result since the density of the beams and the two moments that add to give the torsional stiffness are still being considered on the updating process. The 7th mode shape is also not paired in this attempt due to the lack of understanding on what is happening in the experimental mode shape — which can suggest the presence of errors on either the data acquisition or post processing of data.

Starting with a CCABS of 31.6%, using E, ρ, A, I_y and I_z as parameters to be updated, one has a total of 445 DVs. The model updating process converged after just 3 iterations to a value of CCABS$_{final}$ = 0.69%. Results can be seen in Table 3.7.

Table 3.7: Results obtained for a last model update based on frequencies.

Mode #	f_{EMA} (Hz)	$f_{FEA_{E,\rho,A,I_y,I_z}}$ (Hz)	Δ_f (%)
1	10.34	10.36	0.19
2	35.28	34.86	-1.19
3	50.38	49.51	-1.73
4	81.34	81.21	-0.16
5	129.80	129.93	0.10
6	142.72	143.91	0.83

As expected, by disregarding the 7th mode shape, not only was the final CCABS lower but it also took less iterations to reach the convergence value. Similarly, the reduction on the number of DVs did not contribute to a higher number of iterations before convergence nor did it jeopardize the final result.

For this last attempt, the variations for each of the parameters free to change are plotted in Fig.3.5. The DVs are presented from the root to the tip of the wing, meaning there are masses on the central beam varying from 1 to 25, another 25 for the leading edge and 25 more for the trailing edge. For the beam, there are beams connecting the 25 central masses (DV 1 to 24), 25 connecting the central masses to the leading edge ones and another 25 connecting the central masses to the trailing edge.
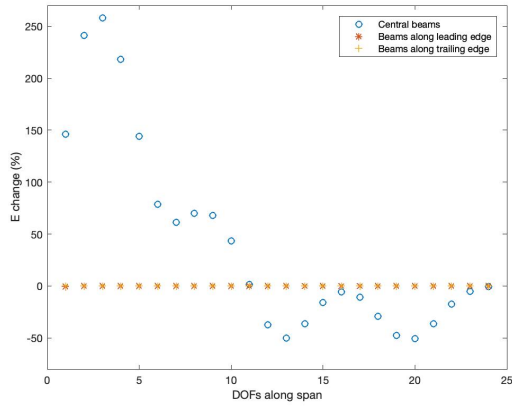
(a) Change on E.
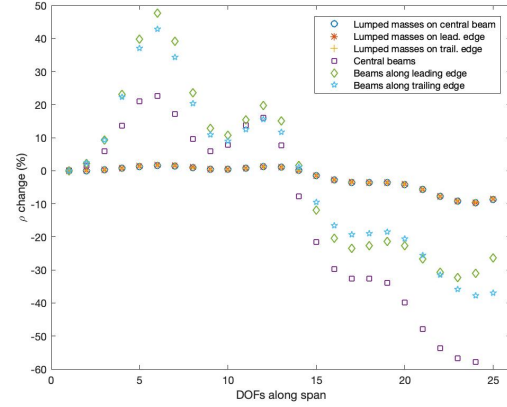
(b) Change on ρ.
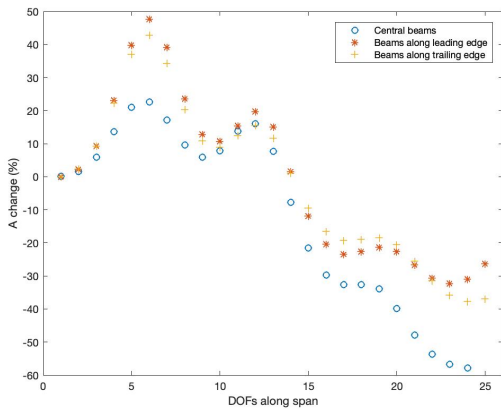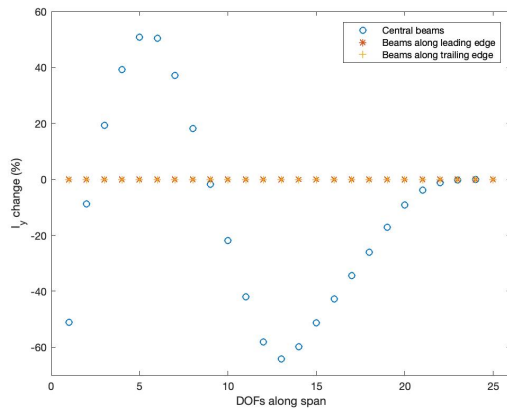
(c) Change on A.

(d) Change on I_y.
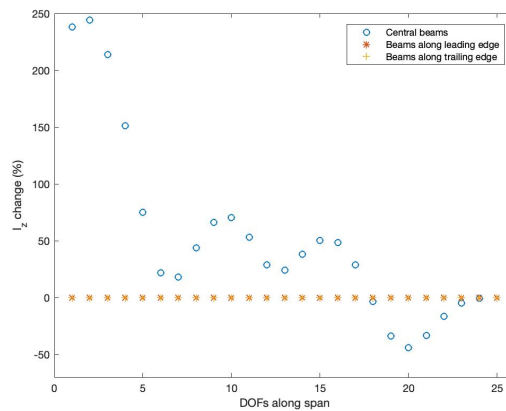
(e) Change on I_z.

Figure 3.5: Results obtained from model updating the FEM.

3.3.2 Updating Based on Mode Shapes

Having succeeded with the matching of frequencies, the same is attempted to be achieved with mode shapes. This proved to be a more challenging task, as will be discussed through the remaining of this chapter.

Since the focus now is on a broader aspect of modal analysis, the mode shapes, the CC chosen to be converged while model updating is the CCTOTAL. The 7th mode shape will no longer be considered as it has shown to be extremely difficult to match the frequency of as explained previously.

Prior to any model update it is important to analyze what the MAC matrix looks like so that one can see how it is evolving with each of the attempts for making it converge into an ideal one — which would have the diagonal values close to unity and the off-diagonal ones close to zero. Fig.3.6 shows a top view of the MAC matrix before any model update had been performed.
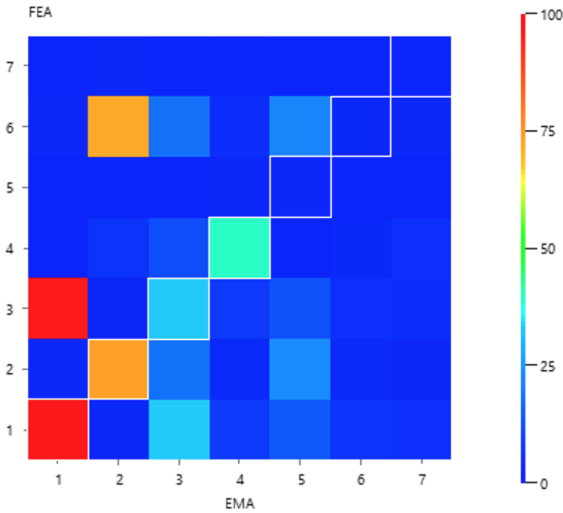
Figure 3.6: MAC matrix before any model update.

The mode shape pairing was performed in a sequential order, meaning that the 1st mode shape obtained from EMA is paired with the 1st mode shape from FEA and so on as seen in Table 3.8.

Table 3.8: MAC values before any model update for each of the mode shape pairs.

Mode shape pair #	EMA mode #	FEA mode #	MAC (%)
1	1	1	97.0
2	2	2	73.2
3	3	3	32.7
4	4	4	39.2
5	5	5	1.5
6	6	6	2.3
7	7	7	0.5

As expected, the 7th experimental mode shape is not consistent with the 7th mode shape derived from the beam model. Moreover, it is not consistent with any of the other mode shapes. A similar

phenomenon is also now evident when referring to the 5th experimental mode shape. The 6th mode shape pair also presents a very low MAC and for these reasons, the initial focus will lie on the matching of the 1st, 2nd, 3rd and 4th mode shape pairs.

CCTOT convergence

Similarly to the frequency matching, different combinations of parameters were chosen to update for a better understanding of how the CC would evolve. The chosen ones were the following:

- Updating of E.

- Updating of E and ρ.

- Updating of E, ρ, A, I_y and Iz.

After running *FEMtools*, the results obtained are shown in Table 3.9. MAC values for each of the mode shape pairs considered, the number of DVs there are in each of the attempts and the number of iterations it took for convergence to be reached are also presented. Even though CCTOT was the CC set to converge, the contribution of CCABS and CCMAC was also extracted for a clearer picture of how frequency matching and mode shape matching happened.

Table 3.9: Results obtained when attempting to converge CCTOT.

Mode shape pair #	MAC_i (%)	MAC_E (%)	$\text{MAC}_{E,\rho}$ (%)	$\text{MAC}_{E,\rho,A,I_y,I_z}$ (%)
1	97.02	94.72	95.73	93.93
2	73.20	67.04	67.99	67.57
3	32.75	38.25	36.57	28.88
4	39.27	42.30	39.97	43.05
# DVs	—	74	223	445
# Iterations	—	6	4	10
CCTOT	80.01	50.02	50.76	42.35
CCABS	40.57	10.59	10.82	0.69
CCMAC	39.44	39.42	39.93	41.66

From the results obtained, it is interesting to notice that the most complex mode shape pair among the ones considered — the 4th mode — was the one to see its MAC increased in all different attempts.

Despite CCTOT showing a significant decrease, it does not necessarily translate into a decrease in CCMAC, but instead a convergence of the frequencies. Since this is not what was meant to be studied — and will essentially correspond to the study done in the beginning of this chapter — the approach to it had to change.

Alternatively, CCMAC could be tried to converge, letting the natural frequencies adjust freely.

CCMAC convergence

The previous study was then repeated but setting *FEMtools* so that it would try to minimize the value of CCMAC. This was done using the same sets of parameters — firstly E alone, secondly adding ρ and lastly with E, ρ, A, I_y and Iz. This would provide the same circumstances in terms of DVs and therefore ease taking conclusions.

The results obtained can be seen in Table 3.10.

Table 3.10: Results obtained when attempting to converge CCMAC.

Mode shape pair #	MAC_i (%)	MAC_E (%)	$\text{MAC}_{E,\rho}$ (%)	$\text{MAC}_{E,\rho,A,I_y,I_z}$ (%)
1	97.02	94.96	95.73	94.30
2	73.20	67.40	67.99	68.63
3	32.75	37.96	36.57	29.04
4	39.27	42.03	39.97	41.65
# DVs	—	74	223	445
# Iterations	—	5	4	9
CCTOT	80.01	50.01	50.76	42.57
CCABS	40.57	10.68	10.82	0.97
CCMAC	39.44	39.41	39.93	41.59

Once again, *FEMtools* was not able to approximate the behavior of the simplified FEM to the wing. In fact, the CCMAC did not suffer significant changes. Instead, the software appears to match the frequencies again, even when no constraint was applied to them.

Noise reduction

To further investigate whether the lack of consistency between the mode shapes was due to misuse of the software, misuse of the MAC as a criterion to compare the data, due to experimental or post-processing errors that might have happened during the testing phase or even due to the choosing of a poor FEM to start the model update process with — which can be true if, for instance, there are not enough DVs in the model for convergence of frequencies and mode shapes all at once — noise in the experimental data was reduced.

This was done by approximating the three first out-of-plane mode shapes — EMA mode shapes number 1, 2 and 4 — by polynomial fitting. Two different polynomials were found for each of the mode shapes (one for the leading edge and the second for the trailing edge) and put into a .uff format so that it could be read by *FEMtools*. The results obtained for the MAC between these and the FEA mode shapes can be seen in Table 3.11.

Judging by these results, there was significant noise in all these mode shape experimental extractions. In fact, for the fourth mode shape pair the initial MAC almost doubled, showing that, even though it is actually a 3rd out-of-plane bending mode shape, its extraction or data post-processing did not account for the noise there was.

Table 3.11: Comparison between MAC before and after polynomial regression applied to the experimental data.

Mode shape pair #	MAC_i (%)	$\text{MAC}_{i_{\text{reg}}}$ (%)
1	97.02	99.61
2	73.20	84.26
4	39.27	74.30

One last time, reducing CCMAC to lower values was attempted using *FEMtools*. For this one, only these mode shape that had been interpolated were considered. Again, this showed to be not successful, even with the noise reduction for these three modes and updating the maximum number of DVs possible.

All these results lead one to think that either a simplified model constituted by beams and lumped masses is not ideal for describing a wing's behavior and therefore there is no solution for the problem as it was formulated or that the software itself is incapable of performing the required task without being biased towards matching the frequencies over matching the mode shapes.

Therefore, when model updating the aircraft in Chapter 6, a different approach will be tried for the mode shape matching.

Control Iteration

The control iteration served the purpose of checking how good (or bad) of an approximation the points where the lumped masses of the FEM were from the place where DOFs from GVT on the wing were.

To do so, the eigenvectors for each mode shape obtained from the FEM were extracted and put into the EMA file that is used as input on *FEMtools*. This was done in such a way that the displacement of the experimental DOF and the closest modal mass of the FEM to that DOF was the same. In this way, the only reason for the MAC matrix not to have the diagonal elements close to 100% and the off-diagonal elements close to 0% is the fact that the offset on the coordinates from the DOFs and FEM lumped masses can make mode shapes to appear incoherent when they are not. The MAC matrix obtained can be seen in Fig.3.7.

The values for the diagonal of this matrix are shown in Table 3.12.

Table 3.12: MAC values for diagonal mode shape pairs from control iteration.

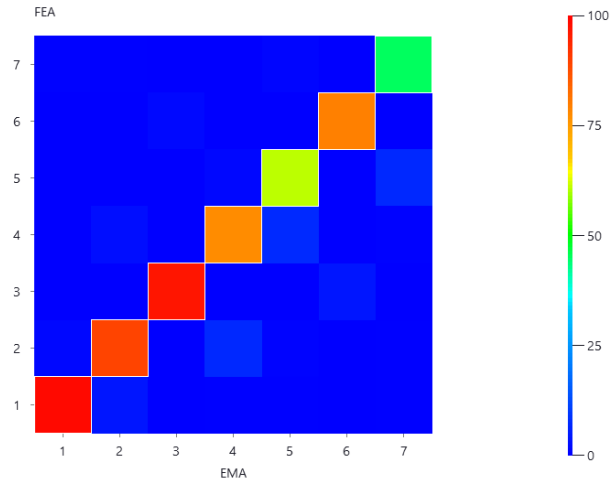| EMA mode #	FEA mode #	MAC (%)
1	1	98.4
2	2	88.8
3	3	96.5
4	4	77.1
5	5	60.4
6	6	79.1
7	7	44.8

Figure 3.7: MAC matrix when setting FEM mode shapes data into experimental DOFs.

All off-diagonal elements of the matrix are now bellow 10% and the main diagonal ones above 40% and in most cases above 75%. As expected, these results were the best obtained so far. They demonstrate much more consistency than the ones obtained in previous tries and can pinpoint some flaws in the approximating of the FEM mass points to the chosen DOFs. Actually, the DOFs chosen by Araújo were also not ideal, in the sense they are not distributed along straight lines throughout the leading and trailing edges nor in the same spatial planes. This being said, it becomes an extremely laborious task developing a simple model that has almost no offset between experimental and computational DOFs.

These results also corroborate the initial idea that mode shape pairs between the 5th EMA mode and the 5th FEA mode, as well as between the 7th EMA mode and 7th FEA mode were not suited to be studied, as they present a MAC lower than 65% even in these circumstances.

Just as an attempt to get even more satisfactory results, the 'MAC Contribution Analysis' functionality of the software was used to find which of the 50 DOFs contributed more for the reduction of the MAC values on the main diagonal so that those could be disregarded. These results can be seen in Fig.3.8.
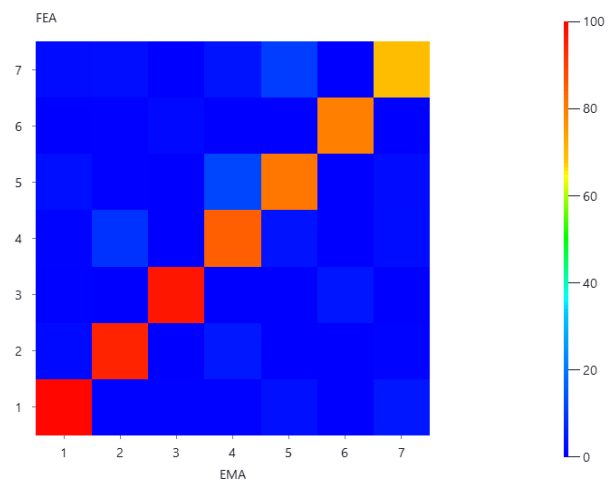

Figure 3.8: MAC matrix for control iteration after disregarding the 16 less coherent node pairs.

The values for the diagonal of this matrix are presented in Table 3.13.

Table 3.13: MAC values for mode diagonal mode shape pairs for control iteration after disregarding the 16 less coherent node pairs.

EMA mode #	FEA mode #	MAC (%)
1	1	99.0
2	2	94.3
3	3	96.5
4	4	84.5
5	5	80.8
6	6	79.1
7	7	69.2

Again having all the off-diagonal matrix elements bellow 10%, the results obtained when disregarding the 16 points that most reduce the average main diagonal MAC below 100% verify the hypothesis that the software and methodology are being correctly used.

As expected the MAC increased for most of the mode shape pairs, averaging at 86.2% for the main diagonal elements when considering roughly $2/3$ of the most consistent DOFs.

The reason for a decrease in successive mode shape pairs — from 99.0% for the 1st mode shape pair to 69.2% for the 7th one — can be explained by the the physical distance between the position of the sensors and the mass points on the FEM that are closest to them, which has an average value of 4.65cm at undeformed position. Since the intricacy of mode shapes increases over the mode number, this small distance can scale to bigger values on higher mode shapes, making the mode shapes less and less coherent between themselves.

Chapter 4

Experimental Testing and Data Post-Processing Procedures

As preparation for GVT on the assembled aircraft, tests on a wing structure specimen were performed. This choice had to do with the simplicity of a wing compared to a complete aircraft, and since the time slot allocated for performing the GVT on the aircraft was brief, it was considered to be the best option for getting familiarized with all the data acquisition equipment and software so that when the time for the actual testing would come, it could go as smoothly as possible.

The goal here was to get acquainted with the process of extracting the FRFs for the proposed DOFs and be able to visualize the mode shapes of the wing structure. By doing so, one can then visually compare them with the computational predictions within the time frame available, so that further calculations and modal updating can be performed without taking the risk of the obtained data being flawed or compromised — which would be critical given the unavailability of the aircraft for further testing.

This chapter focuses on the preparation and considerations taken for the GVT as well as on the description of the tests made prior to them.

4.1 Assumptions

The assumptions taken into account before performing the test itself include the following:

- Impact testing was chosen to be performed, as opposed to the shaker testing for reasons already stated in subsection 2.2.2.

- The roving hammer method was adopted, rejecting the option of roving the sensors, for the higher time efficiency of the former technique.

- The free-free boundary condition was simulated by hanging the wing by a rope from above and even if not perfect, it was found to be the most practical solution. The number of detected Rigid Body Motion (RBM) oscillations will be lower than in an ideal free-free scenario but the mode

shapes remain unchangeable as long as there is no overlapping of the previous two on the FRF spectra.

- The soft hammer tip was selected since the range of frequencies of interest does not extended to higher frequencies than 150-200Hz.

4.2   Data acquisition equipment and software

The equipment used for the tests described in the current and following chapters include:

- One ICP Impact Hammer Model 086C03 with adjustable tips that make it possible to vary the hardness of the hammer. The tip used for these tests was the black one, which is, according to the user manual description, a 'soft impact cap'. The range to choose from goes from super soft impact to hard impact and all the mentioned above can be seen in Fig.4.1(a).

- One IEPE NI 9234 acquisition card, to which the hammer and two accelerometers were connected, as seen in Fig.4.1(b).

- Two PCB Piezotronics Accelerometers Model 352A24 as seen on Fig.4.1(c). Their placement was done in such a way that they would collect both in-plane and out-of-plane information depending on the direction of the hammer hit.

- One rope for hanging the wing — which was considered to be the best way of simulating the desired boundary condition with the available means. The wing's setup can be seen in Fig.4.1(d). The frequencies at which the RBM oscillations appear depend on the length of the rope but the natural frequencies do not. For this reason, it can be varied in order to shift them if found necessary.

Meanwhile, a *LabVIEW* interface was developed in order to collect the information coming from both the impact hammer and the two sensors through the DAS. By doing so, two FRFs were able to be saved at each recording, corresponding to the output of the two sensors divided by the input of the hammer. Each FRF is saved in a .uff file format containing its real and imaginary parts.

To make sure the impact transmitted to the wing is as similar as possible to a Dirac's delta, a filter in the time domain with a band of 10ms was applied to the hammer input signal, so that in the case it would touch the surface of the structure more than once or if the impact was longer than what was considered to be reasonable for results accuracy, *LabVIEW* would reject the measurements.

The averaging of three successful impacts is then to be obtained for every recording. The recording is only to be saved and further analyzed when the coherence for the frequency range of interest is above 0.9. If not, the recording of another three successful impacts is to be redone for that same DOF.

4.3   Wing Specimen GVT

Due to the simplicity of the structure to be studied and the introductory character of this first experiment, only 18 points were chosen to be tested, divided throughout the leading and trailing edges. Given the
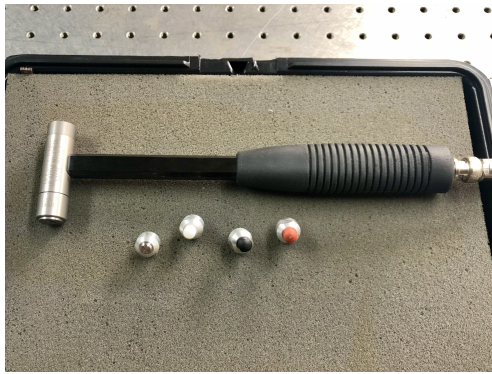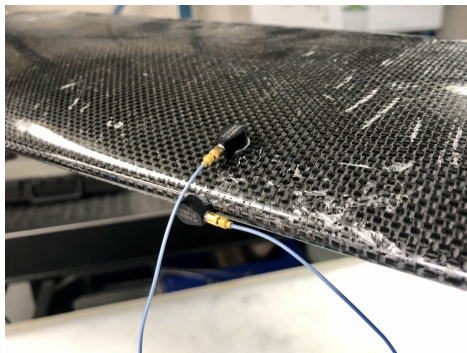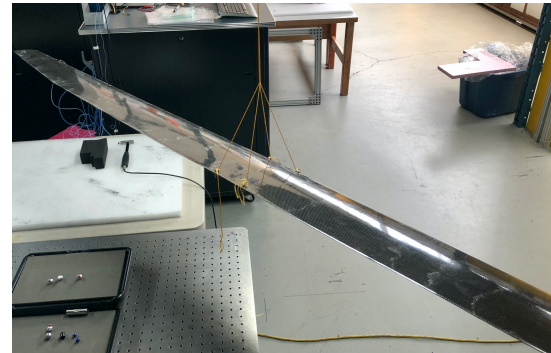
(a) Impact hammer and tips to choose from.

(b) DAS setup for tests on morphing wing.

(c) Detail of sensor placement on wing specimen.

(d) Wing setup for free-free boundary condition.

Figure 4.1: Equipment and setup for GVT tests performed on a wing specimen.

geometry of the wing, the 9 points on the leading edge could be tested for both out-of-plane and in-plane vibration modes, while the remaining ones on the trailing edge were tested for in-plane vibrations only. The total of 27 DOFs were then collected and the number of FRFs obtained was double that value — since there are two sensors collecting data from the impacts at any time.

In Fig.4.2 one can see the simplified model created on *MEscope* for the wing specimen. Points are numbered from 1 to 18, corresponding to the order in which they were impacted. Points 1 to 5 and 15 to 18 are on the leading edge whereas points 6 to 14 are on the trailing edge of the wing. As for point 19, it corresponds to the position of the sensors, one positioned so that it collects out-of-plane data and the other so that it collects in-plane data. No data is extracted at this location and for that reason the software's interpolation capabilities may be used when visualizing the mode shapes for point 19.

Once all FRFs were collected, the model generated on *MEscope* was now able to be animated. To do so, each of the FRF had to be associated to the specific DOF where the hammer had hit while taking into account which sensor had collected that FRF.

4.3.1 Modal parameters extraction

Through *MEscope* one can now extract modal parameters such as the natural frequencies, damping and mode shapes for the wing. Doing so is possible by overlaying the FRFs for out-of-plane and later for in-plane data. After examining the magnitude spectra of these FRFs one can easily predict and approximate the structure's resonant frequency thanks to the peaks appearing consistently on several of them.
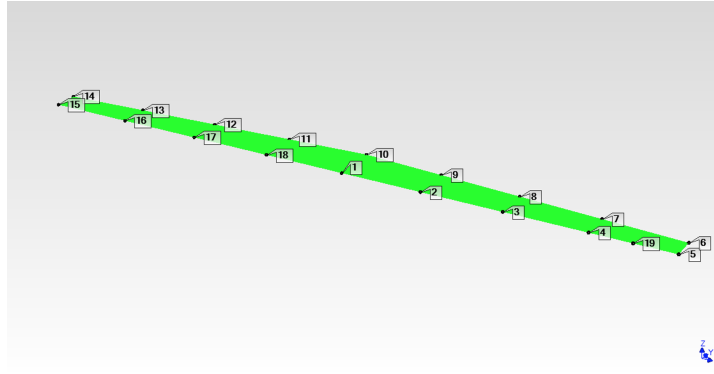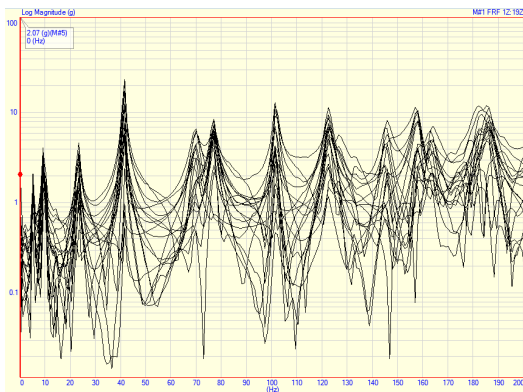
37

Figure 4.2: Generated model in *MEscope* for the wing specimen.

Nonetheless, mathematical algorithms present in the software allow a more accurate approximation for the natural frequencies and damping.

Fig.4.3 corresponds to the overlaid magnitude spectra of the collected FRFs for out-of-plane vibrations — along z axis — and for in-plane vibrations — along y axis.

(a) FRFs for out-of-plane direction — z axis.
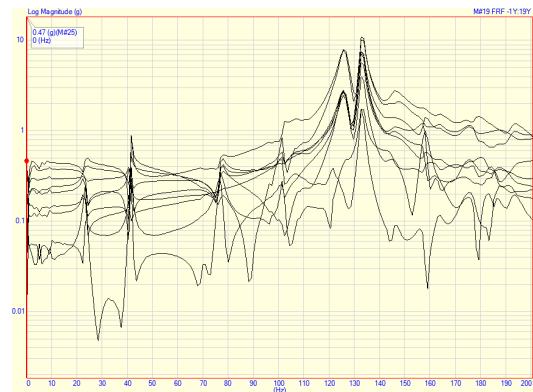
(b) FRFs for in-plane direction — y axis.

Figure 4.3: Overlaid amplitude spectra of FRFs for both out-of-plane and in-plane directions.

Presented in Table 4.1, the modal parameters extracted using *MEscope* capabilities correspond to eight out-of-plane mode shapes — from #1 to #6, #9 and #10 — and two in-plane mode shapes — #7 and #8.

These values for natural frequencies and damping are obtained by zooming in into the a range of frequencies surrounding the frequency one is trying to check and, by making use of one of the 'mode indicator' functionalities — which applies a method such as the Complex Mode Indicator Function (CMIF) —, one can be sure whether the peak corresponds to a resonant frequency of not. For the case of accelerations, the imaginary part is the one to be taken into account when running CMIF and immediately after that a Local Polynomial method is used to compute the frequencies and damping shown before. *MEscope* allows to further save the mode shapes corresponding to these frequencies and damping after calculating the residues of these polynomials.

Even though there are peaks located at frequencies lower than the ones detected as corresponding to natural frequencies, these correspond to RBM oscillations for the out-of-plane spectra. As for the

Table 4.1: Natural frequencies and damping for detected mode shapes.

Mode #	f_{EMA} (Hz)	ζ_{EMA} (%)
1	23.0	2.34
2	41.3	0.647
3	69.8	2.07
4	76.9	1.32
5	102	0.726
6	123	0.916
7	126	0.714
8	133	0.586
9	146	0.900
10	158	0.916

in-plane spectra, they are due to interference of the out-of-plane mode shapes, that were still measured by the sensor placed at an in-plane direction.

In fact, one can easily check this last fact when overlaying both sets of spectra, ending up with several of the resonant peaks from the out-of-plane spectra matching exactly those also detected in-plane, even though the latter do present a lower magnitude (as it is expected *a priori*). This phenomenon emphasizes the fact there is human error involved in impact hammer testing and in the sensor placement process. Getting the direction of the hammer to be exactly the same as the one the sensor is facing at every single measurement is virtually impossible, specially with sensors as sensitive as the ones used.

Nevertheless, this kind of results are satisfactory and do not compromise any study that should follow. As long as the modal analysis peaks are filtered and selected conscientiously, valid results can be expected.

4.3.2 Wing Specimen Mode Shapes

The mode shapes were obtained and animated with *MEscope*. Out-of-plane mode shapes can be seen in Fig.4.4 and in-plane mode shapes in Fig.4.5.

All first symmetric and anti-symmetric bending and torsion modes appear and can be seen clearly. The frequencies are widely spread and therefore there is no interference between different mode shapes. Interpolating the 19th point (correspondent to the sensor), the curves describing the mode shapes are smooth enough for the number of DOFs chosen to be appropriate. Moreover, the sensor placement was adequate, hence it is not siting on any node of the obtained mode shapes.

These ten first resonant frequencies identified for the wing include two in-plane ones that can only be visualized on the leading edge. The trailing edge should present a similar behavior at the same frequency of 126Hz for the 1st bending and 133Hz for the 2nd bending.

The wing's model updating study could now follow but a similar one has already been done for the BA wing on the previous chapter of this thesis.
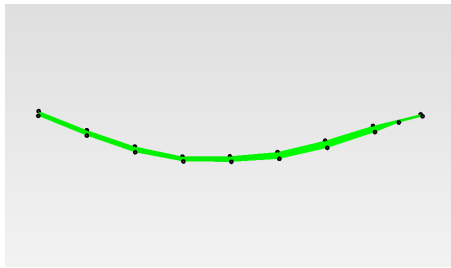
(a) 1st bending — 23.0 Hz.
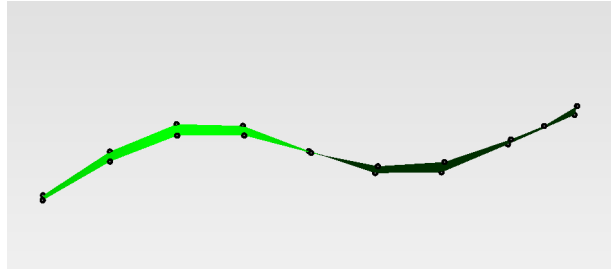
(b) 1st bending anti-symmetric — 41.3 Hz.
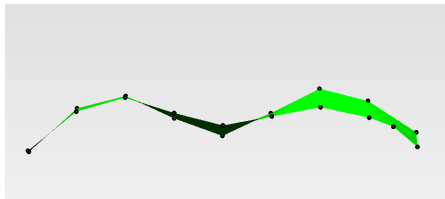
(c) 2nd bending — 69.8 Hz.
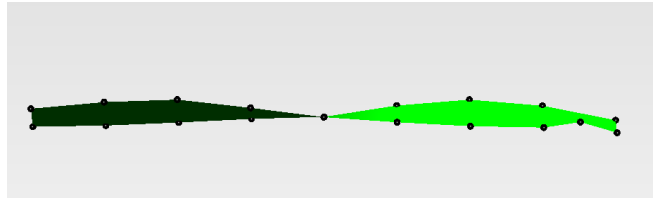
(d) 1st torsion — 76.9 Hz.
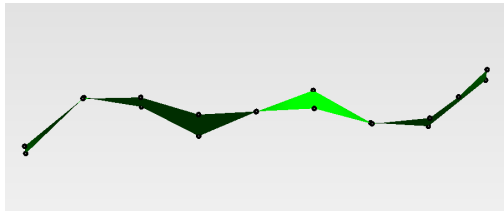
(e) 2nd bending anti-symmetric — 102 Hz.
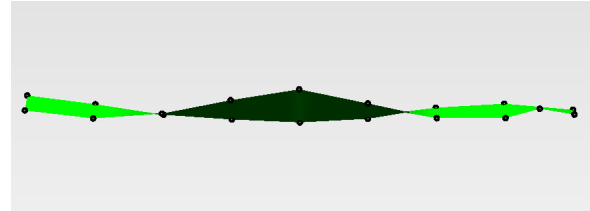
(f) 2nd torsion — 123 Hz.
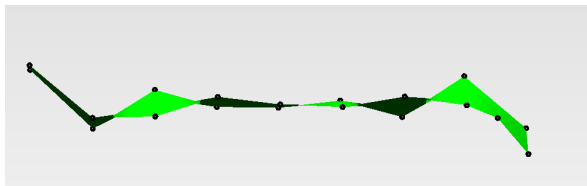
(g) 3rd bending anti-symmetric — 146 Hz.
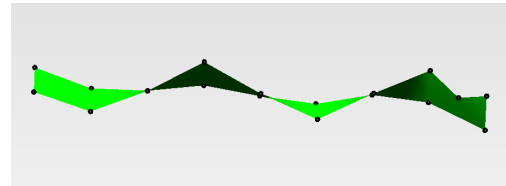
(h) 3rd torsion — 158 Hz.

Figure 4.4: Out-of-plane mode shapes obtained from GVT on morphing wing.
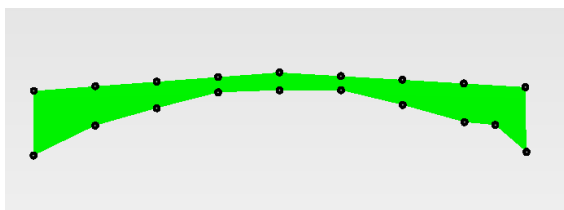
(a) 1st bending — 126 Hz.
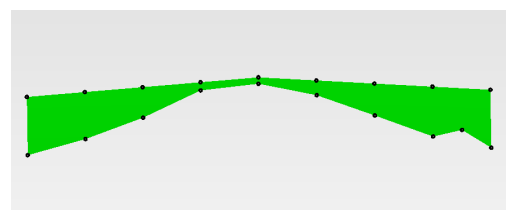
(b) 2nd bending — 133 Hz.

Figure 4.5: In-plane mode shapes obtained from GVT on morphing wing.

The same procedure will be mimicked but involving a higher level of complexity when performing GVT on the BA aircraft since there are multiple structures and coupling between mode shapes may appear in different ones. Some other considerations should be addressed and comments are to be made throughout the next chapter.

Chapter 5

Ground Vibration Testing

Once the time for performing ground tests on the aircraft had come, everything had to be performed with the maximum efficiency possible so that the aircraft could proceed to the flight testing phase.

Preparations for GVT included analyzing the previously developed FEM of the aircraft and consequently the choosing of locations where the sensors were to be placed. *MEscope*'s model was developed before the tests so that the FRFs could be added to the software and the experimental mode shapes examined rapidly. This had to be done fast enough to decide whether or not DOFs were to be added and if some of the extractions had to be repeated.

The results from the analytical model predicted a first symmetrical bending mode shape at 5.6Hz and if testing showed that the first elastic mode was actually substantially lower than that, it could have been critical to some of the control algorithms of the aircraft's autopilot.

The overall procedure required performing two different testing sessions. The need for both of them, their procedure and the results obtained are discussed throughout the rest of this chapter.

5.0.1   Assumptions, Equipment and Software

The equipment used for the aircraft's GVT is similar to that used on the wing specimen. Some adaptations to better suit this case regarding instrumentation and software used were:

- Four acquisition cards were used instead of one. In order to collect data from all 15 sensors and the hammer simultaneously, three extra cards were connected to the DAS — Fig.5.1(a).

- Given the extra mass and inertia of the aircraft of the aircraft when compared to the wing specimen, an extra mass was added to the impact hammer for a clearer extraction of the input signal — Fig.5.1(b).

- The model generated through *MEscope* was a simplified representation of the aircraft. All points tested on the wings and horizontal stabilizer were assumed to be coplanar. The same principle was applied to each of the individual winglets and vertical stabilizers — Fig.5.2.

- The DOFs chosen to hit the hammer on were marked with a whiteboard marker, measured according to the dimensions introduced for the *MEscope* model.

(a) DAS collecting data from 15 sensors and impact hammer.

(b) Impact hammer with soft tip and extra mass added.

Figure 5.1: Setup of used equipment during testing on the 16.5% model aircraft.
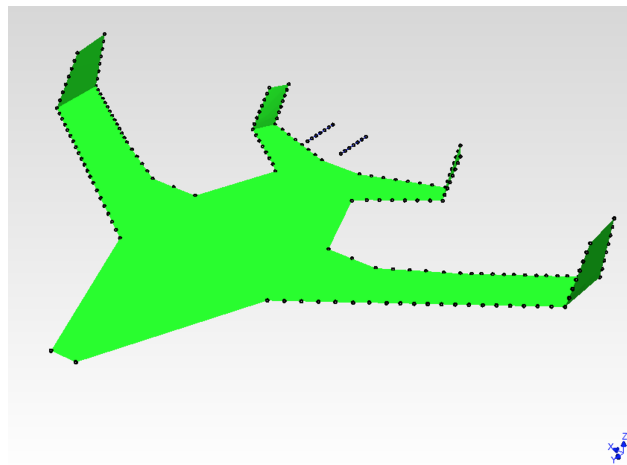
Figure 5.2: *MEscope* model for the aircraft.

- The nacelles of the aircraft were only tested in one direction, making use of the fin above them to mark the DOFs.

- Once again the option of hanging it by a cable was chosen to simulate the free-free boundary condition. This time two cables were used, elevating the aircraft from its supports, positioning it at about 1m from the floor for Test #1. As for Test #2, the aircraft was supported by one cable alone, elevating it 5cm above the ground.

- The *Labview* interface used for the wing specimen test was improved to acquire the data from 15 sensors and the impact hammer simultaneously.

- A previously developed FEM of the assembled aircraft was used to predict which mode shapes would be detected and at what frequency. For that purpose, the modal masses of the mode shapes that resulted from *Ansys*' modal analysis were considered.

5.1 Test #1

Test #1 was the most extensive one. A total of 186 locations were marked across the aircraft over the wings, winglets, horizontal stabilizer, vertical stabilizers and nacelles. These were numbered as seen in Table 5.1 and after analyzing the FEM, the wings, winglets and the horizontal stabilizer were decided to be studied for in-plane vibrations as well. For this reason, the overall number of DOFs totalized 230.

Table 5.1: Marks on aircraft structures for Test #1.

Mark #	Structure	Out-of-plane	In-plane
1 to 21	Right wing at leading edge	✓	✓
22 to 42	Right wing at trailing edge	✓	—
43 to 63	Left wing at leading edge	✓	✓
64 to 84	Left wing at trailing edge	✓	—
85 to 91	Right winglet at leading edge	✓	✓
92 to 98	Right winglet at trailing edge	✓	—
99 to 105	Left winglet at leading edge	✓	✓
106 to 112	Left winglet at trailing edge	✓	—
114 to 120	Right horizontal stabilizer at leading edge	✓	✓
122 to 128	Right horizontal stabilizer at trailing edge	✓	—
130 to 136	Left horizontal stabilizer at leading edge	✓	✓
138 to 144	Left horizontal stabilizer at trailing edge	✓	—
145 to 151	Right vertical stabilizer at leading edge	✓	—
152 to 158	Right vertical stabilizer at trailing edge	✓	—
159 to 165	Left vertical stabilizer at leading edge	✓	—
166 to 172	Left vertical stabilizer at trailing edge	✓	—
173 to 179	Right nacelle	✓	—
180 to 186	Left nacelle	✓	—

As stated before, the aircraft was hanged from the ceiling — Fig.5.3(a) — by two cables. Doing so allowed it to rise from the styrofoam supports and an equilibrium position was reached once the aircraft was supported by the cables under tension. Fig.5.3(b) shows in more detail the way in which the aircraft was supported by the cables.

Sensors were placed as shown in Table 5.2. Once more, no FRFs were measured at these DOFs and for that reason *MEscope*'s capabilities had to be used to interpolate their displacement on the mode shapes. The data of adjacent points was averaged based on the distance they are from the sensor points and smooth mode shapes were obtained. The choosing of these marks to place the sensors had to do with the structures to be studied and again the necessity of not having them placed on nodes of the mode shapes of interest.

Each successful group of three hits in any of the aircraft's structure resulted in 15 FRFs saved. The extractions were considered to be successful if the coherence between the three hits were above 0.9 for the range of interest — which for the case of the aircraft was for frequencies up to 100Hz. For that reason, one selected the soft tip of the hammer for testing.

Fig.5.4 combines photos showing the marks and sensors placed on the aircraft. Special attention

(a) Mechanism to hang aircraft from ceiling.

(b) Connection between aircraft and cables.

Figure 5.3: Setup of aircraft for Test #1.

Table 5.2: Sensor placement for Test #1.

Sensor #	Mark #	Direction	Structure	Type
1	19	z	Right wing	Out-of-plane
2	19	y	Right wing	In-plane
3	90	$-x$	Right winglet	Out-of-plane
4	90	y	Right winglet	In-plane
5	119	z	Right horizontal stabilizer	Out-of-plane
6	119	y	Right horizontal stabilizer	In-plane
7	150	$-x$	Right vertical stabilizer	Out-of-plane
8	177	x	Right nacelle	Out-of-plane
9	61	z	Left wing	Out-of-plane
10	61	y	Left wing	In-plane
11	104	x	Left winglet	Out-of-plane
12	104	y	Left winglet	In-plane
13	135	z	Left horizontal stabilizer	Out-of-plane
14	135	y	Left horizontal stabilizer	In-plane
15	164	x	Left vertical stabilizer	Out-of-plane

had to be given to the cables connecting the sensors to the DAS this time. Any rougher oscillation of the aircraft or disruption on its equilibrium could lead to the sensors to move slightly, compromising the results.

The FRFs for the left nacelle were obtained once the extraction of the rest of the data was complete. Sensor #8 was removed from the right nacelle and used on the left nacelle at mark #184.

Once the extraction of all FRFs was complete, the computational work of attributing each of the FRFs to the *MEscope* model could be done.

Before that, so that the idea that both landing gears would not be a problem for the integrity of the aircraft during flight tests could be corroborated, their first natural frequencies were also determined by placing one sensor on the nose landing gear and two sensors on the main landing gear — one for out-of-plane and the other in-plane motion. In fact, by analyzing the output of *Labview*, the first resonant
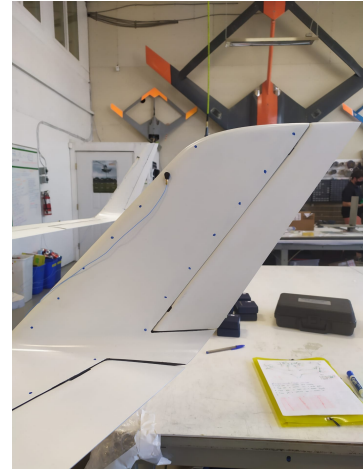
(a) Marks and sensors on winglet.

(b) Marks and sensors on horizontal stabilizer.

(c) Marks and sensor on vertical stabilizer.

(d) Marks and sensors on wing.

(e) Marks and sensor on nacelle.

Figure 5.4: Detail of sensors placed over the structures of interest.

frequency for the nose landing gear was estimated to be occurring at approximately 70.1Hz, while the out-of-plane one for the main landing gear was occurring at 25.6Hz and the in-plane one at 56.2Hz.

5.1.1 Test #1 Results

After going through the procedure explained in the previous chapter, the results obtained for the first seven resonant frequencies are presented in Table 5.3. The relative differences between these and the results obtained using a FEM were also computed.

The aircraft appears to be generally stiffer in bending and torsion when compared to the FEM according to the differences obtained for the natural frequencies of the first modes. In fact, the FEM went through several mass updates as the development phase of the aircraft progressed but its stiffness did not suffer a final adjustment once the aircraft was assembled, which explains this shift on the lower resonant frequencies.

Each of these experimental mode shapes were then animated and matched with the appropriate analytic mode shapes and are described next.

Table 5.3: Computational and experimental natural frequencies.

Mode #	f_{FEA} (Hz)	f_{EMA_1} (Hz)	Δf (%)
1	5.57	6.68	+19.93
2	9.00	10.27	+14.11
3	13.97	14.48	+3.65
4	17.82	20.59	+15.54
5	21.95	23.47	+6.92
6	27.23	24.60	-9.66
7	29.87	25.67	-14.06

Mode Shape #1

The first experimental mode shape detected using *MEscope*'s capabilities — Fig.5.5(b) — occurred at a frequency of 6.68Hz and corresponds to a 1st wing symmetrical bending out-of-plane mode shape. Its natural frequency is 19.93% higher than initially estimated and it matches the first FEA mode shape obtained through *Ansys* — Fig.5.5(a) —, which had a modal mass of 4.20.

(a) 1st FEA mode shape.   (b) 1st EMA mode shape.
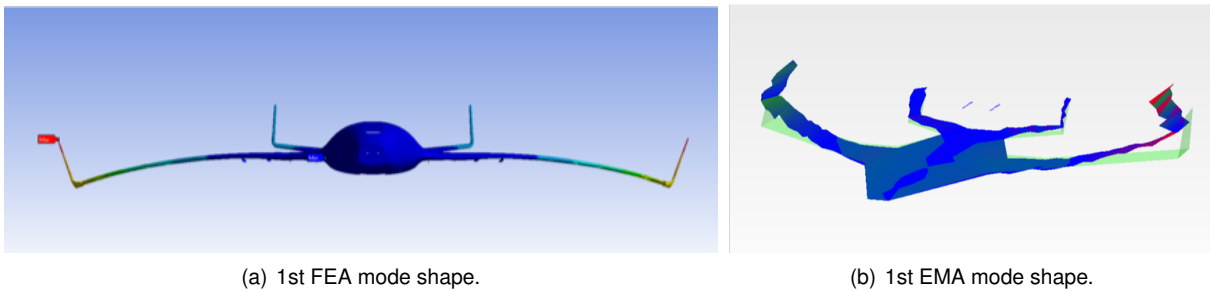
Figure 5.5: 1st wing symmetrical bending out-of-plane.

Mode Shape #2

The second EMA mode shape — Fig.5.6(b) — matches the second obtained from FEA — Fig.5.6(a). It is the 1st out-of-plane wing anti-symmetrical bending mode shape, happening at 10.27Hz — a 14.11% higher frequency than computationally predicted. Its modal mass, at 3.18, was inferior to that of the first mode shape, contributing less to the overall deformation of the aircraft.

(a) 2nd FEA mode shape.   (b) 2nd EMA mode shape.

Figure 5.6: 1st out-of-plane wing anti-symmetrical bending.

Mode Shape #3

The third mode shape is a horizontal stabilizer one. In fact, the 1st out-of-plane horizontal stabilizer anti-symmetrical bending mode shape is both the third mode shape detected by analytical — Fig.5.7(a) — and experimental methods — Fig.5.7(b). Analytically, it is found at 13.97Hz, whereas experimentally at 14.48Hz — a shift of +3.65%.

(a) 3rd FEA mode shape.   (b) 3rd EMA mode shape.
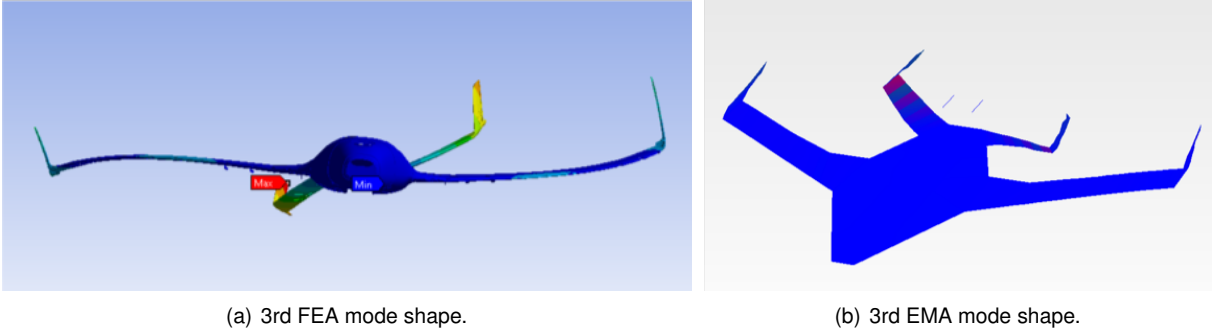
Figure 5.7: 1st out-of-plane horizontal stabilizer anti-symmetrical bending.
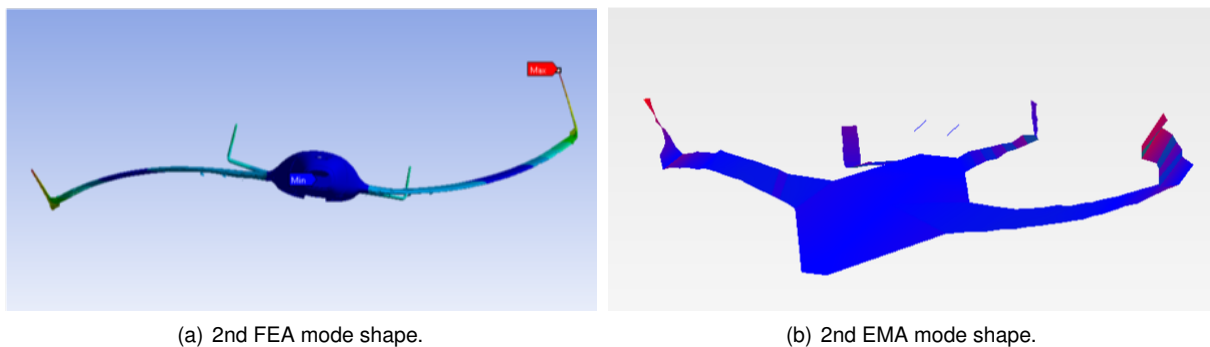
Mode Shape #4

The fourth mode shape found by EMA — Fig.5.8(b) — has as its parallel the seventh analytical mode shape — Fig.5.8(a). This has to do with the fact that FEA's mode shapes #4 to #6 have negligible modal masses and for that reason contribute very little to the overall deformation of the aircraft's structures. Consequently, these mode shapes were not detected experimentally. The FEA natural frequency is 17.82Hz while the one detected by experiments was 20.59Hz — an increase of 15.54%. It corresponds to the 2nd out-of-plane wing symmetrical bending.

(a) 7th FEA mode shape.   (b) 4th EMA mode shape.

Figure 5.8: 2nd out-of-plane wing symmetrical bending.

Mode Shape #5

The fifth EMA mode shape — Fig.5.9(b) — is the 1st wing torsion mode shape, which for the reason explained in the previous pair of mode shapes, also suffers a shift in the number of the analytical one. At an experimental resonant frequency of 23.47Hz, it is 6.92% above that from FEA — Fig.5.9(a).
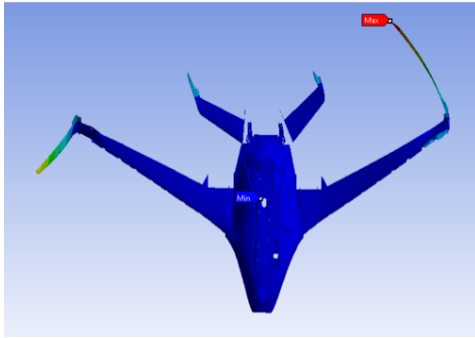
(a) 10th FEA mode shape.
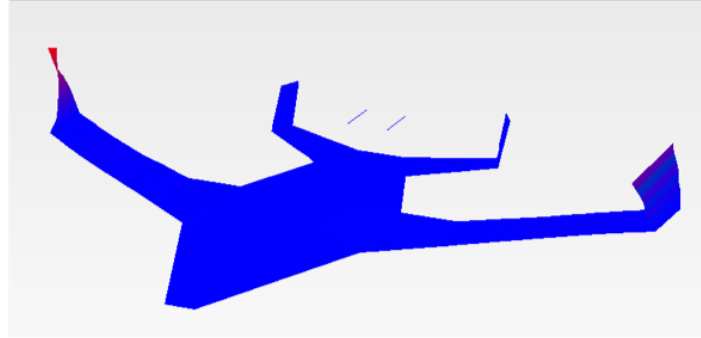
(b) 5th EMA mode shape.

Figure 5.9: 1st wing torsion mode shape.

Mode Shape #6

The sixth mode shape is the 1st in-plane horizontal stabilizer anti-symmetrical bending. Through EMA — Fig.5.10(b) — it exhibits a natural frequency of 24.60Hz, a value 9.66% below the FEA one — Fig.5.10(a) —, which was the 13th analytical one.
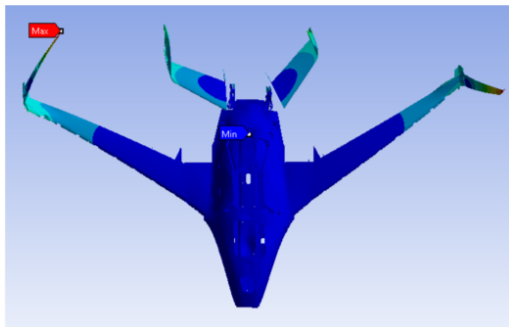
(a) 13th FEA mode shape.
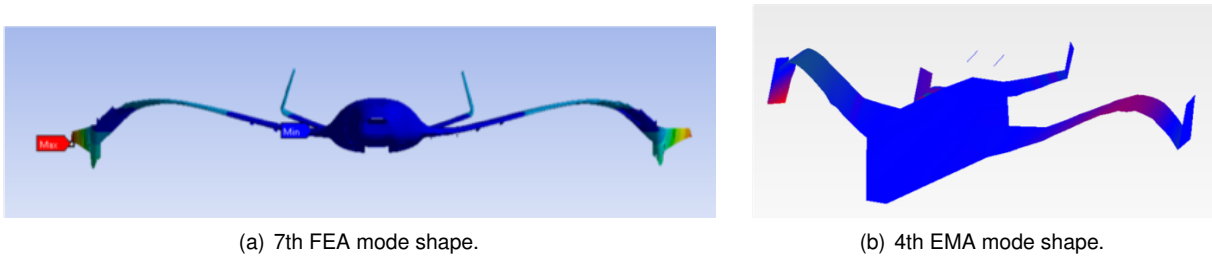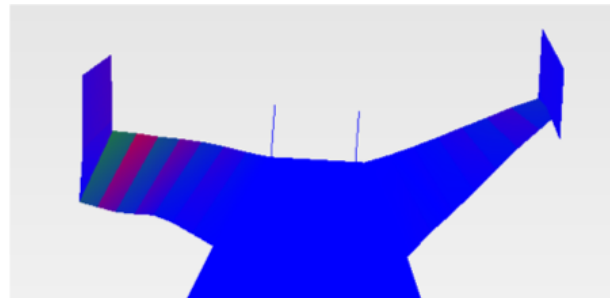

(b) 6th EMA mode shape.

Figure 5.10: 1st in-plane horizontal stabilizer anti-symmetrical bending.

Mode Shape #7

The seventh mode shape obtained through *MEscope* — Fig.5.11(b) — was a match of the 18th analytical one — Fig.5.11(a). Being 14.66% apart, the experimental one was found at 25.67Hz while the FEA one at 29.87Hz and it corresponds to the 2nd wing torsion mode shape.
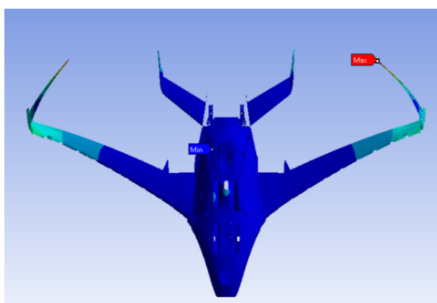
(a) 16th FEA mode shape.

(b) 7th EMA mode shape.

Figure 5.11: 2nd wing torsion mode shape.

48

5.2 Test #2

Once the mode shapes were identified there was still the uncertainty on whether or not the peak appeared on the FRF spectra for a frequency slightly bellow the 6.88Hz mode shape was actually an RBM oscillations and not elastic deformation. The question rose from the fact that when animating this peak in *MEscope*, it presented a behavior of RBM but also some bending on the tip of the wings. For this reason, a second testing session was performed.

Overall a simpler test, the number of spots marked on the aircraft this time was reduced to 29. They were spread across both wings and the fuselage as shown in Table 5.4.

Table 5.4: Marks on aircraft structures for Test #2.

Mark #	Structure
1 to 5	Right wing at leading edge
6 to 10	Right wing at trailing edge
11 to 15	Left wing at leading edge
16 to 20	Left wing at trailing edge
21 to 29	Fuselage

Once again hanging from the ceiling, this time the aircraft was supported by one single cable at a closer position relatively to the ground. This was predicted to shift the RBM oscillations and not interfere with the natural frequencies and would be the most expedite way of confirming if the peaks showing in the FRF spectra for frequencies below 6.68Hz were actually related to RBM. Fig.5.12 shows the setup of the aircraft for Test #2.

(a) Aircraft ready for Test #2.
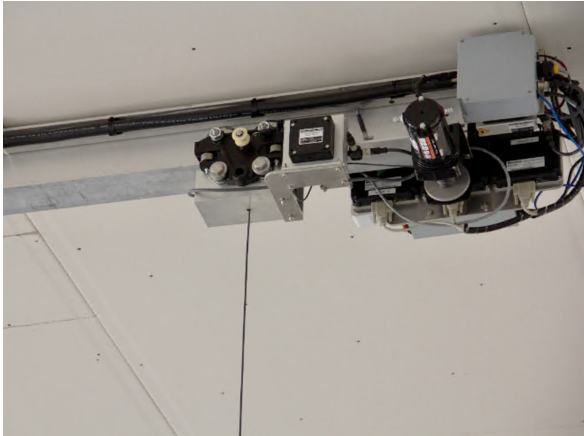
(b) Detail of mechanism to hang aircraft.

Figure 5.12: Setup of aircraft for Test #2.

As explained for Test #1, the places where sensors were placed had to be later interpolated and their distribution is shown in Table 5.5. Most of the sensors are now placed on the fuselage since no mode shape of the fuselage is to be detected at such low frequencies, meaning that the RBMs will be visible on the sensors without much coupling of elastic deformation.

Table 5.5: Sensor placement for Test #2.

Sensor #	Mark #	Direction	Structure	Type
1	4	z	Right wing	Out-of-plane
2	4	y	Right wing	In-plane
3	22	x	Fuselage (front)	In-plane
4	22	y	Fuselage (front)	Axial
5	22	z	Fuselage (front)	Out-of-plane
6	28	x	Fuselage (back)	In-plane
7	28	z	Fuselage (back)	Out-of-plane

5.2.1 Test #2 Results

The data collected during Test #2 was later processed and the results compared with the ones obtained for the first testing session. The comparison of the first natural frequencies can be seen in Table 5.6.

Table 5.6: Natural frequencies for both testing sessions.

Mode Shape #	f_{EMA_1} (Hz)	f_{EMA_2} (Hz)	Δf_{EMA} (%)
1	6.68	6.55	-1.95
2	10.27	10.20	-0.69
3	14.48	14.51	+0.21
4	20.59	20.38	-1.03
5	23.47	23.72	+1.05
6	24.60	—	—
7	25.67	25.83	+0.62

No resonant frequency was detected for mode shape #6 since it was an in-plane mode shape affecting the horizontal stabilizer and this new distribution of sensors and DOFs did not show an evident peak for that structure in the vicinity of the frequency range it was supposed to be identified.

As can be seen in the table, all of the detected mode shapes happen at a frequency that is within a 2% margin for both testing sessions. Such results show that, as predicted, there was no major shift in these peaks. Also supporting that, the shift in frequency is happening to both lower and higher frequencies depending on the mode shape number, showing no consistency.

As for the question regarding RBM oscillations, the FRF spectra for both tests were also compared visually and then post-processed. With that intent, the frequencies at which the RBM oscillations are detected were calculated once more through *MEscope*'s algorithm explained in the previous chapter.

Fig.5.13 shows both magnitude FRF spectra for test #1 and test #2. As predicted, the RBM oscillations shifted to lower frequencies, making them easier to analyze.

The values obtained through *MEscope* for these frequencies are shown in Table 5.7. From the results obtained and by animating the RBM peaks, motions resembling pitch and heave behaviors are detected and the elastic deformation on the tip of the wings previously detected on the second RBM on test #1 is no longer appearing in test #2.

The first RBM saw its frequency decreased by 11.32% while the second one decreased 43.71% from

(a) Overlaid magnitude FRF spectra for Test #1.

(b) Overlaid magnitude FRF spectra for Test #2.
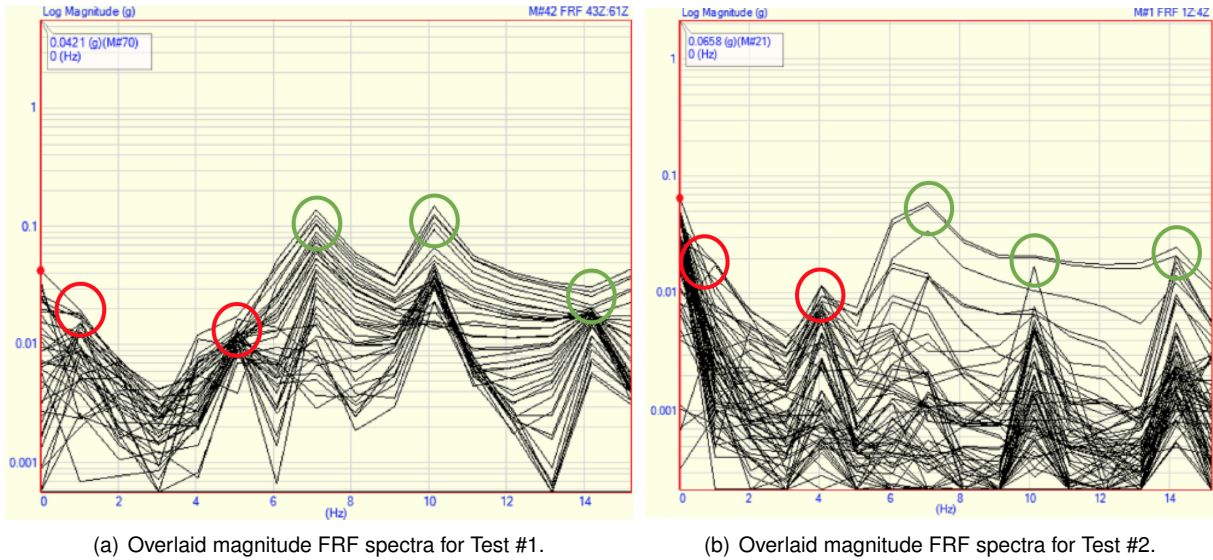
Figure 5.13: FRF spectra for both testing sessions. In red RBM oscillations and in green elastic deformations.

Table 5.7: Frequencies of RBM oscillations for both tests.

Test #	f_{RBM_1} (Hz)	f_{RBM_2} (Hz)
1	0.59	4.80
2	0.53	3.34

changing the boundary condition. This explains why the tip of the wings is not deforming anymore. In fact, the decrease in the frequency of the second RBM was enough to stop the interference between this RBM and the first mode shape.

Having confidence that the lower frequencies detected in Test #1 are indeed corespondent to RBM oscillations, one can now be surer that the elastic deformations will not compromise the behavior of the aircraft's avionics system during flight.

Chapter 6

Aircraft Model Update

Having accomplished the main goals of the testing phase, the model updating study can now begin. An attempt at frequency matching proved to be successful by making use of *FEMtools*. As for the mode shapes, a different approach was tried, using an optimization algorithm developed in *MATLAB*.

In this chapter, the simplified FEMs developed using *Ansys APDL* are described explored and attempts at matching their modal parameters discussed.

6.1 Frequency Matching

Similar to the procedure explained in Chapter 3 for the wing, convergence of frequencies between a simplified FEM created on *Ansys APDL* — Fig.6.1(a) — and the data extracted from GVT was attempted. The generated model was made of 19 different beam sections on the fuselage, 25 describing each wing, 15 for each side of the horizontal stabilizer and 10 for both winglets and each of the vertical stabilizers.

The experimental results, after being extracted from *MEscope* as amplitude and phase for each DOF and each mode shape, had to be converted to their real and imaginary parts and put in a .uff format so that they could be imported to *FEMtools*.

Once that was done, the node pairing for the experimental DOFs and the FEM nodes was computed and is shown in Fig.6.1(b). The mode shapes were paired sequentially, meaning EMA mode shape #1 is paired with FEA mode shape #1 and so on.

(a) Aircraft simplified FEM developed in *Ansys*.   (b) Node-point pairs obtained from *FEMtools*.
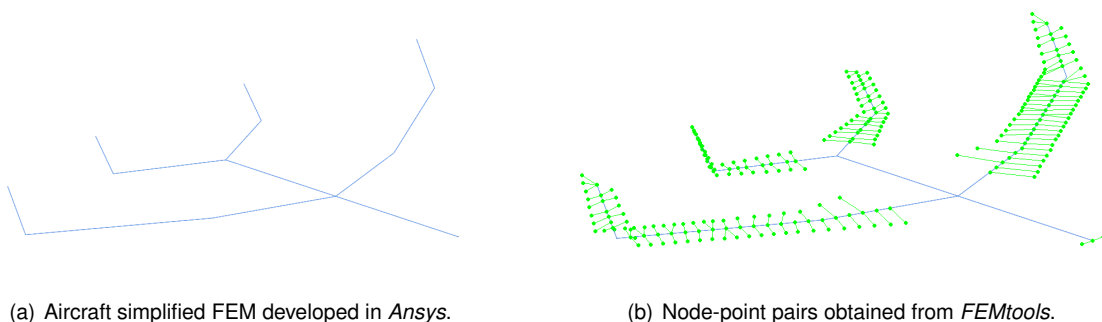
Figure 6.1: FEM and node-pairs between FEM and experimental model.

The study focused on out-of-plane mode shapes and disregarded the mode shape identified as in-plane on the horizontal stabilizer at 24.60Hz. For that reason, the mode shape previously coined as #7 is now #6. A comparison between the experimental and analytical natural frequencies before any update is presented in Table 6.1.

Table 6.1: Comparison between EMA and FEA natural frequencies before model updating.

Mode #	f_{EMA} (Hz)	f_{FEA} (Hz)	Δ_f (%)
1	6.68	7.71	+15.41
2	10.27	10.44	+1.66
3	14.48	11.68	-19.34
4	20.59	16.49	-19.91
5	23.47	24.32	+3.62
6	25.67	25.99	+1.25

This time, four different attempts to match frequencies were made and the parameters to be updated in each of them were the following:

- Updating of E.

- Updating of ρ.

- Updating of A.

- Updating of I_y and I_z.

After having a CCABS of 10.2% to start the iterative loop with, *FEMtools* converged to 0.88% when updating E alone after seven iterations and having 139 DVs to update the values of. This satisfied the required constraint of having CCABS lower than 1% better than any of the other sets of parameters and for this reason it was found to be enough for satisfactory results when wanting to match frequencies. Therefore there is no need to add any extra structural parameters or increase the complexity of the FEM's geometry.

In fact, the convergence criterium reached for the other attempts was the one where two consecutive values of CCABS are within a margin of 0.1, leading to a value of CCABS higher than 1%. The results obtained for all these attempts are presented in Table 6.2.

Table 6.2: Comparison of number of DVs, number of iterations and CCABS$_{final}$ between different parameters update.

Update of	# DVs	# Iterations	CCABS$_{final}$ (%)
E	139	7	0.88
ρ	139	14	1.3
A	139	14	1.3
I_y, I_z	278	5	4.8

Fig.6.2 shows the evolution of CCABS until convergence was reached and the iterative loop stopped for the attempt in which E was chosen to update alone.
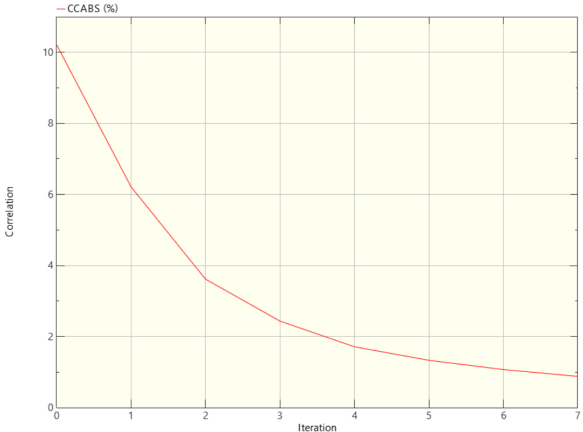

Figure 6.2: Evolution of CCABS when updating E.

All FEM's resonant frequencies are now within a margin of 1.5% of the correspondent experimental natural frequencies — Table 6.3.

Table 6.3: Results obtained for a model updating E on *FEMtools*.

Mode #	f_{EMA} (Hz)	f_{FEA_E} (Hz)	Δ_{f_E} (%)
1	6.68	6.69	+0.15
2	10.27	10.23	-0.39
3	14.48	14.36	-0.83
4	20.59	20.30	-1.41
5	23.47	23.37	-0.42
6	25.67	26.29	-1.48

These results can also be seen graphically and are shown in Fig.6.3.

(a) Frequency matching before update — CCABS = 10.2%.
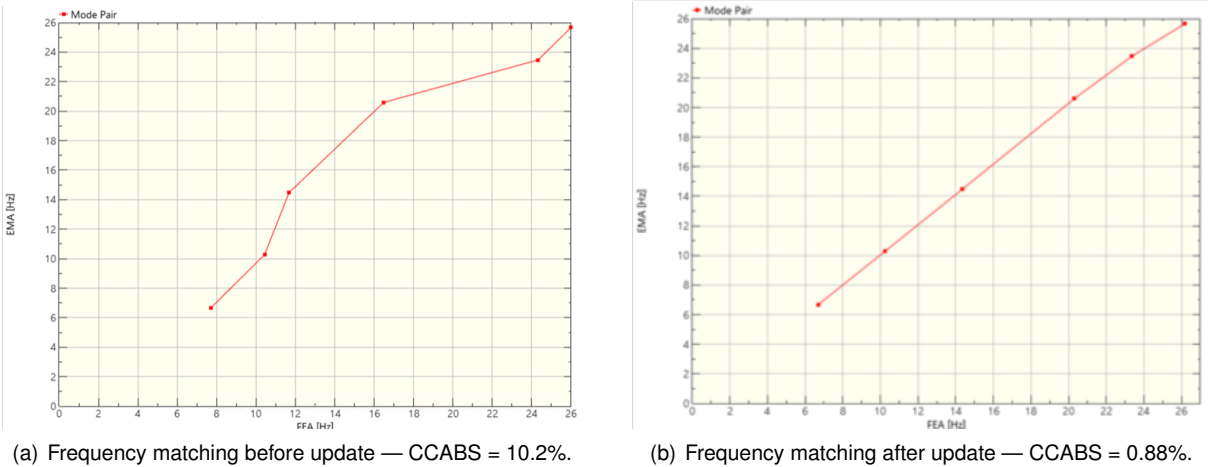
(b) Frequency matching after update — CCABS = 0.88%.

Figure 6.3: Comparision between frequency matching before and after E update.

The DVs suffered the biggest updates in the fuselage elements, followed by the horizontal stabilizer and wings. Both winglets and vertical stabilizers saw their first elements — the ones closer to the

horizontal stabilizers and the wings respectively — change much more than all their others. Results are shown in Fig.6.4.
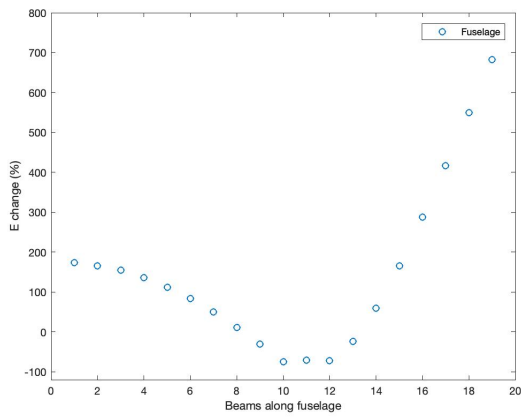
(a) E change on fuselage elements.
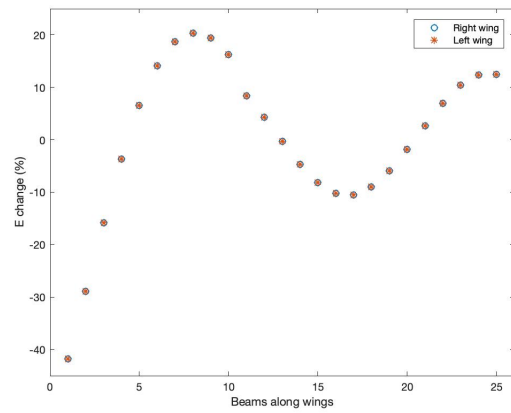
(b) E change on wing elements.
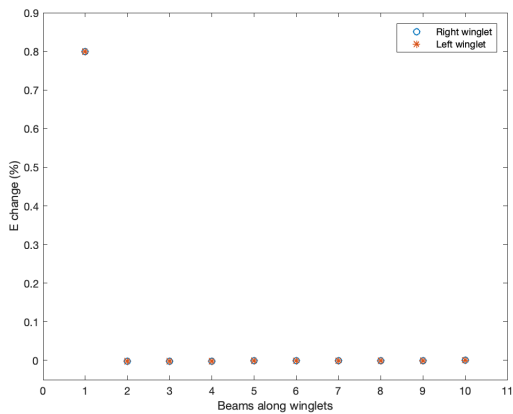
(c) E change on winglet elements.
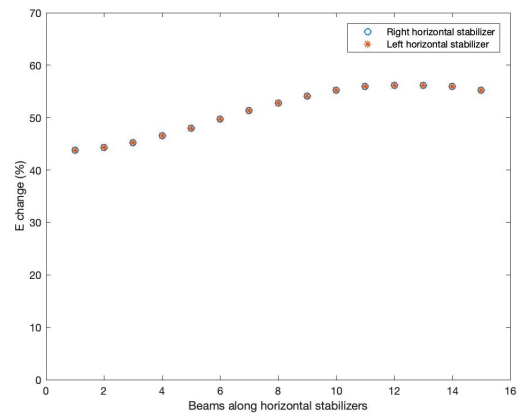
(d) E change on horizontal stabilizer elements.
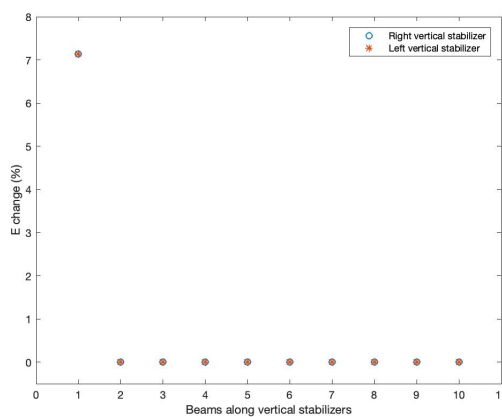
(e) E change on vertical stabilizer elements.

Figure 6.4: Results obtained from model updating of the aircraft's FEM.

The matching of frequencies for the aircraft showed to be easier than the one studied for the wing in Chapter 3, with 139 DVs updated 7 times, as opposed to 445 DVs updated during 3 iterations.

6.2 Mode Shape Matching

As an attempt to develop and explore a more methodic way to converge mode shapes between experimental and analytical data, the mode shape matching was approached by an optimization algorithm developed in *MATLAB*. As many other optimization problems, this one can be generically formulated as follows:

$$
\begin{aligned}
\text{Minimize} \quad & f(\mathbf{x}) \\
\text{w.r.t.} \quad & \mathbf{x} \in \chi, \\
\text{subject to} \quad & g_i(\mathbf{x}) \leq 0, \ i = 1, ..., m \\
& h_j(\mathbf{x}) = 0, \ j = 1, ..., l \, .
\end{aligned}
\tag{6.1}
$$

where $\mathbf{x} = [x_1, x_2, ..., x_n]^T$ is the column vector of real-valued design variables and is member of the feasible set of design points χ, f is the objective function to be minimized and $\mathbf{g}$ and $\mathbf{h}$ are the vectors of inequality and equality constraints respectively.

To accomplish that, *MATLAB*'s *fmincon* function was used and lower and upper bounds established to constrain the DVs of the generated models in *Ansys APDL*.

The goal here was to maximize the MAC between certain pairs of mode shapes. Since *fmincon* function minimizes f, the latter was chosen as being the symmetric of a weighted sum of the MAC between corresponding mode shapes. From equation 2.17, it is evident the need of extracting the modal vectors from both analytical and experimental mode shapes before the MAC could be computed. Once done, the model updating study proceeded with an initial attempt at matching the 1st out-of-plane symmetric bending mode shape.

No equality constraints were imposed but the natural frequencies of the FEM were constrained by forcing them to be inside an interval centered on the EMA's resonant frequencies of the corresponding experimental mode shapes with a maximum deviation of 10%. Mathematically

$$
\begin{aligned}
f_{\text{FEA}_i}(\mathbf{x}) \in [0.9, 1.1] \cdot f_{\text{EMA}_i} \Rightarrow \Delta_{f_i}(\mathbf{x}) = \left| \frac{f_{\text{FEA}_i}(\mathbf{x}) - f_{\text{EMA}_i}}{f_{\text{EMA}_i}} \right| \leq 0.1 \\
\Rightarrow g_i(\mathbf{x}) = \Delta_{f_i}(\mathbf{x}) - 0.1 \leq 0,
\end{aligned}
\tag{6.2}
$$

where i corresponds to the mode shape pair to be matched.

6.2.1 1st out-of-plane symmetric bending mode shape

To begin with, the 1st out-of-plane symmetric bending mode shape is attempted to converge. To do so, a higher complexity model was generated comparatively to the one discussed in the beginning of this chapter. Multipoint Constraint (MPC) elements were added to the FEM in order to connect the nodes along the beams previously made to the nearest points where the experimental DOFs were located.

Adding to that, the cross section of the beam elements is now tubular rectangular.

A total of 17 design variables were chosen and were updated throughout the running of the algorithm. Their description can be seen in Table 6.4.

Table 6.4: DV description for first attempt at converging 1st out-of-plane symmetric bending mode shape.

DV #	Description
1	E on fuselage's beam elements
2	E on wings' beam elements
3	E on horizontal stabilizers' beam elements
4	E on winglets' beam elements
5	E on vertical stabilizers' beam elements
6	Outer width of the wing's box at the root
7	Outer height of the wing's box at the root
8	Outer width of the wing's box at the tip
9	Outer height of the wing's box at the tip
10	Outer width of the winglet's box at the tip
11	Outer width of the winglet's box at the tip
12	Ratio between thickness of webs and outer width of the box at wing's root
13	Ratio between thickness of webs and outer width of the box at wing's tip
14	Ratio between thickness of webs and outer width of the box at winglet's tip
15	Ratio between thickness of skins and outer height of the box at wing's root
16	Ratio between thickness of skins and outer height of the box at wing's tip
17	Ratio between thickness of skins and outer height of the box at wing's tip

Once convergence was reached, the results were the ones shown in Table 6.5. The best outcome was obtained after 115 iterations for a MAC of 45.57%, an increase of 35.52% from the initial value. The feasibility criterium was satisfied since the relative difference between experimental and analytical natural frequencies for this mode shape was lower than 10%.

Table 6.5: Evolution on frequency and MAC for 1st out-of-plane symmetric bending mode shape — first attempt.

Iteration #	MAC_1 (%)	f_{FEA} (Hz)	Δ_f (%)	Feasible
0	35.10	2.44	-63.47	—
115	47.57	6.67	-0.15	✓

The MAC was computed by extracting the modal vectors from the nodes at the end of each of the generated MPC elements, which have the same coordinates as the experimental DOFs when both are at their undeformed position. By comparing these with the corresponding modal vectors from the experimental DOFs through equation 2.17, *fmincon* was able to minimize the value of $-MAC_1$.

The resulting mode shape after model updating can be seen and compared in Fig.6.5.

Though the MAC between experimental and analytical mode shapes increased for the 1st out-of-plane symmetric bending one, results below 60% are usually not satisfactory enough to assume consistency between two mode shapes. For that reason, more freedom was given to the FEM model as an
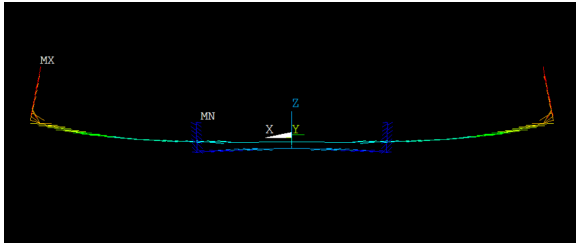
(a) FEM mode shape #1 — front view.
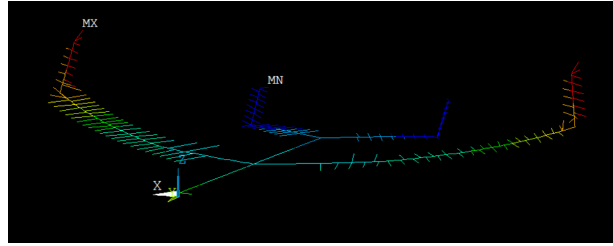
(b) FEM mode shape #1 — isometric view.

(c) EMA mode shape #1 — front view.
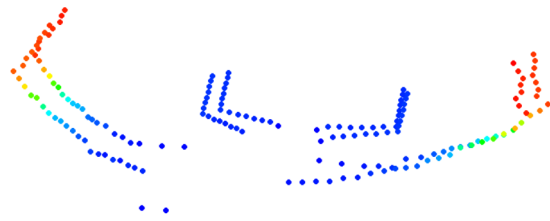
(d) EMA mode shape #1 — isometric view.

Figure 6.5: 1st out-of-plane symmetric bending mode shape — $f_{\mathsf{FEA}} = 6.67 Hz$ and $\mathsf{MAC}_1 = 47.57\%$.

attempt to improve results.

This time, masses were place at the end of the MPC elements and a linear distribution of masses simulated for the wing between the root and kink and between the kink and tip and for the winglet, horizontal and vertical stabilizers between the root and tip. The added DVs are compiled in Table 6.6.

Table 6.6: Additional DV for matching of 1st out-of-plane symmetric bending mode shape.

DV #	Description
18	Mass on wing's root at leading edge
19	Mass on wing's kink at leading edge
20	Mass on wing's tip at leading edge
21	Mass on winglet's root at leading edge
22	Mass on wing's root at trailing edge
23	Mass on wing's kink at trailing edge
24	Mass on wing's tip at trailing edge
25	Mass on winglet's root at trailing edge
26	Mass on winglet's tip at leading edge
27	Mass on winglet's tip at trailing edge
28	Mass on horizontal stabilizer's root at leading edge
29	Mass on horizontal stabilizer's tip at leading edge
30	Mass on vertical stabilizer's root at leading edge
31	Mass on vertical stabilizer's tip at leading edge
32	Mass on horizontal stabilizer's root at trailing edge
33	Mass on horizontal stabilizer's tip at trailing edge
34	Mass on vertical stabilizer's root at trailing edge
35	Mass on vertical stabilizer's tip at trailing edge

The structural changes these masses induced put the MAC at a value of 86.26% without any model updating — a very satisfactory value taking into account the starting value of 35.10%. After running the algorithm this increased and converged to an even higher value of 94.09%.

Table 6.7: Evolution on frequency and MAC for 1st out-of-plane symmetric bending mode shape — second attempt.

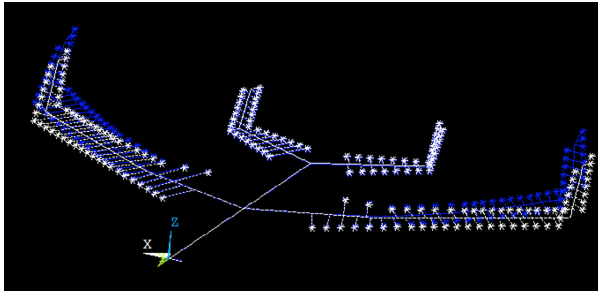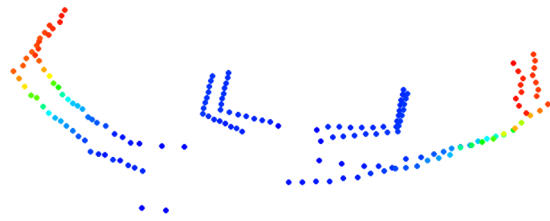| Iteration #	MAC_1 (%)	f_{FEA} (Hz)	Δ_f (%)	Feasible
0	86.26	7.37	+10.33	—
16	94.09	6.66	-0.30	✓

Both undeformed — white — and deformed — blue — configurations can be seen in Fig.6.6 for $MAC_1 = 94.09\%$.

(a) FEM mode shape #1 after addition of masses — isometric view.

(b) EMA mode shape #1 — isometric view.

Figure 6.6: 1st out-of-plane symmetric bending mode shape — $f_{FEM} = 6.66 Hz$ and $MAC_1 = 94.09\%$.

6.2.2 1st torsion mode shape

The next step in the study was the matching of the 1st torsion mode shape. After some unsuccessful tries, extra DVs were added to the formulation of the problem, increasing the complexity of the FEM. This time, the direction of the masses was uncoupled and DVs #18 to #27 were now used as mass DVs on the x direction while 10 new DVs — DVs #36 to #45 — were used as mass DVs on the y direction. For z direction, the distribution was maintained constant at the value that maximized MAC for the 1st out-of-plane symmetric bending mode shape.

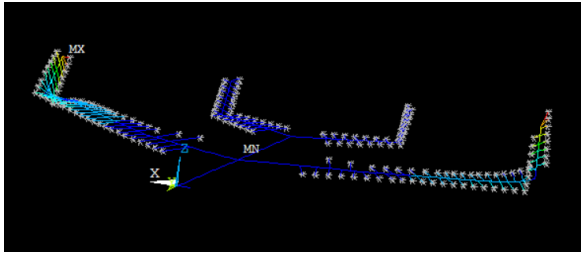Initial values and the optimum obtained results are shown in Table 6.8.

Table 6.8: Evolution on frequency and MAC for 1st torsion mode shape.

Iteration #	MAC_5 (%)	f_{FEA} (Hz)	Δ_f (%)	Feasible
0	14.47	18.34	-21.86	—
53	65.41	22.63	-3.58	✓

The resulting mode shape after the iterative process converged is presented in Fig.6.7.

(a) FEM mode shape #3 — isometric view.

(b) EMA mode shape #5 — isometric view.

Figure 6.7: 1st torsion mode shape — $f_{\mathsf{FEM}} = 22.63 Hz$ and $\mathsf{MAC}_5 = 65.41\%$.

6.2.3 Other attempts

When trying to converge more than one mode shape at a time, little success was achieved.

The optimization of the 1st out-of-plane symmetric bending and the 1st out-of-plane anti-symmetric bending mode shapes simultaneous was able to put the MAC of the former at 89.63% and the latter at 40.55%, an average increase of 38.58% from initial MAC conditions. However, the frequency margin could not be satisfied, compromising the accuracy of this FEM to describe experimental data.

Another attempt involved both 1st out-of-plane symmetric bending and 1st torsion mode shapes. This time, feasibility criteria were satisfied but no improvement was obtained on the average MAC of these mode shapes during the time available to devote to this thesis.

Even though successful at model updating individual mode shapes, the developed optimization algorithm was incapable of a broader convergence of mode shapes given the frequency restriction. This can indicate that more freedom or a refined version of the FEM should be used if interested in proceeding with this study.

Chapter 7

Conclusions and Future Work

This thesis was guided towards two major goals. On one hand, the need to perform Ground Vibration Tests to guarantee the aircraft could proceed to flight testing phase without concerns and on the other hand, the attempt at generating a simplified Finite Element Model capable of matching the dynamic behavior of the aircraft with as little freedom as possible.

While the former was successful and done in an efficient way given the timeframe available, the latter showed to be a much more challenging task. The main conclusions to take from this study as well as suggestions for future work are presented in this last chapter.

7.1   Conclusions

The introductory model update study that took advantage of the GVT data from the aircraft's wing made possible an understanding of how an optimization algorithm can be implemented to match properties between experimental and analytical models. When frequencies were to be matched, *FEMtools* was capable of reducing CCABS from 31.6% to 0.69% by updating E, ρ, A, I_y and I_z. The attempts at mode shape convergence proved to be much more challenging and led to no success. In fact, hardly ever did CCMAC reduce its value during the different tries.

In the meantime, preparations for GVT took place so that the time-consuming tasks that were possible to be done while the aircraft was still unassembled could be done and so that the test procedures and assumptions were established just in time for testing. That involved developing a *LabView* interface that was used for collecting FRFs and may be used in future projects of up to 16 sensors acquiring data simultaneously and the preparation of a *MEscope* model that allowed to compare the analytical results with the ones obtained from experiment as efficiently as possible.

Overall successful, the two test sessions dedicated to GVT required the availability of the aircraft for two and a half days, including marking all the DOFs, extracting the FRFs and making sure the data corresponded to what had somewhat been predicted and therefore the aircraft could be freed and following tests could be done. By performing both sessions, RBMs were identified and the first elastic mode shape found at 6.68Hz, which indicates an apparently stiffer wing than the one predicted

analytically.

Once data was post-processed, the model update study followed firstly for frequency matching by making use of *FEMtools*' capabilities and finally for mode shape matching through an optimization algorithm developed in *MATLAB*. For the former, by updating E alone on a FEM made of beam elements to simulate the aircraft behavior, CCABS was reduced from 10.2% to 0.88% with a total of 139 DVs. As for the latter, more complex FEMs were generated and lead to the convergence of the 1st out-of-plane symmetric bending mode shape and to a significant increase in the MAC of the 1st torsion mode shape of the wings. Nonetheless, when trying to converge multiple mode shapes at once, the algorithm showed to be incapable of solving the problem, demonstrating there is room for adjustments and improvement on both the FEMs and the algorithm itself.

7.2 Future Work

From the work developed in this thesis and presented on this document, a series of ideas on what could follow this study are presented:

- **Optimization algorithm**: Taking advantage of the collected data from GVT and the already developed *MATLAB* optimization algorithm, a broader convergence between the simplified FEM mode shapes and the experimental ones can be attempted so that the dynamic behavior of the aircraft can be represented as accurately as possible. This can be tried by refining the code to take into account that mode shapes can shift during the model updating process, by adding more design variables to the formulation of the problem or by changing the geometry or type of elements to be used through *Ansys*. Nonetheless, it has to be taken into account that the goal here is to have a simplified model and therefore with as little freedom as possible, so some kind of compromise has to be met.

- **Structural analysis**: The mode-superposition method can be applied to characterize the response of the aircraft to transient excitations by using the natural frequencies and mode shapes from the modal analysis.

- **Flutter analysis**: To ensure that the aircraft is free from flutter at all points in the flight envelope, an aeroelastic flutter analysis can be performed once the dynamic behavior of the simplified FEM mimics experimental results.

- **Aeroservoelatic model**: Following the flutter analysis, an aeroservoelastic model can be derived to actively suppress flutter.

Bibliography

[1] C. Humphreys-Jennings, I. Lappas, and D. M. Sovar. Conceptual design, flying and handling quali-
ties assessment of a blended wing body (bwb) aircraft by using an engineering flight simulator, Apr.
2020. School of Engineering, University of South Wales.

[2] R. H. Liebeck. Design of the blended wing body subsonic transport. *Journal of Aircraft*, 41(1):10,
Jan. 2004. doi:10.2514/1.9084.

[3] G. Araújo. Model updating based on static and ground vibration tests of a blended wing body
aircraft. Master's thesis, Instituto Superior Técnico, 2021.

[4] Siemens. Aircraft ground vibration testing: Enhancing the efficiency of aircraft structural dynamics
testing. Software notes, 2020.

[5] Airbus. Imagine travelling in this blended wing body aircraft.
https://www.airbus.com/newsroom/stories/Imagine-travelling-in-this-blended-wing-body-
aircraft.html, 2020. (accessed on June 28th 2021).

[6] Airbus. Airbus reveals new zero-emission concept aircraft.
https://www.airbus.com/newsroom/press-releases/en/2020/09/airbus-reveals-new-zeroemission-
concept-aircraft.html, 2020. (accessed on June 28th 2021).

[7] NASA. Hybrid wing body goes electric. https://www.nasa.gov/content/hybrid-wing-body-goes-
hybrid, 2013. (accessed on June 29th 2021).

[8] D. Rizzo and M. Blackburn. The history of a decision: A standard vibration test method for qualifi-
cation. 2017. Sandia National Laboratories and Stevens Institute of Technology.

[9] U. of Toledo. What is failure, fracture and fatigue? https://www.utoledo.edu/engineering/mechanical-
industrial-manufacturing-engineering/research/fatiguelab/. (accessed on June 30th 2021).

[10] A. Tewari. *Aeroelasticity — Modeling and Control*. Birkhäuser, 1st edition, 2015. ISBN 978-1-4939-
2367-0.

[11] J. He and Z.-F. Fu. *Modal Analysis*. Butterworth Heinemann, 2nd edition, 2001. ISBN 0 7506 5079
6.

[12] C. Instruments. Basics of modal testing and analysis. https://www.crystalinstruments.com/basics-of-modal-testing-and-analysis, 2017. (accessed on May 17th 2021).

[13] M. Peeters, G. Kerschen, and J. C. Golinval. Dynamic testing of nonlinear vibrating structures using nonlinear normal mzodes. *Journal of Sound and Vibration*, 330(3):31, Jan. 2011. doi:10.1016/j.jsv.2010.08.028.

[14] C. Instruments. Applications of experimental modal analysis. https://www.crystalinstruments.com/blog/2017/10/2/applications-of-experimental-modal-analysis, 2017. (accessed on May 19th 2021).

[15] A. Technologies. The fundamentals of signal analysis. Technical report, Agilent Technologies, 2000. Application Note 243.

[16] Siemens. What is a frequency response function (frf)? https://community.sw.siemens.com/s/article/what-is-a-frequency-response-function-frf, 2020. (accessed on May 18th 2021).

[17] A. Technologies. The fundamentals of modal testing. Technical report, Agilent Technologies, 2000. Application Note 243-3.

[18] G. A. Papagiannopoulos and G. D. Hatzigeorgiou. On the use of the half-power bandwidth method to estimate damping in building structures. *Soil Dynamics and Earthquake Engineering*, 31:1075–1079, Feb. 2011.

[19] Brüel and Kjaer. Applications of experimental modal analysis, 2018. Application notes.

[20] E. A. S. Agency. Easy access rules for normal-category aeroplanes cs-23. https://www.easa.europa.eu/sites/default/files/dfu/CS-23%20Amdt%205%20%28AMC-GM%20Issue%201%29.pdf, 2019. (accessed on June 16th 2021).

[21] E. A. S. Agency. Certification specifications for large aeroplanes cs-25. https://www.easa.europa.eu/sites/default/files/dfu/CS-25_Amdt%203_19.09.07_Consolidated%20version.pdf, 2020. (accessed on June 16th 2021).

[22] A. Brandt. *Noise and Vibration Analysis — Signal Analysis and Experimental Procedures*. Wiley, 1st edition, 2011. ISBN 9780470746448.

[23] Siemens. Modal tips: Roving hammer versus roving accelerometer. https://community.sw.siemens.com/s/article/modal-tips-roving-hammer-versus-roving-accelerometer, 2019. (accessed on June 22th 2021).

[24] *FEMtools Model Updating Theoretical Manual*. FEMtools, Interleuvenlaan 64 - 3001 - Leuven - Belgium, 4.1.2 edition, mar 2020.

[25] M. Pastor, M. Binda, and T. Harčarik. Modal assurance criterion, Sept. 2012. Technical University of Košice, Faculty of Mechanical Engineering.

[26] R. J. Allemang. The modal assurance criterion - twenty years of use and abuse, Aug. 2003. University of Cincinnati, Ohio.

[27] SDTools. Mac. https://www.sdtools.com/helpcur/ii_mac.html, 2019. (accessed on May 17th 2021).